SANDIA REPORT

SAND2018-12073
Unlimited Release
Printed October 2018

Multi-configuration Membrane Distillation Model (MCMD)

Daniel L. Villa, Johan Vanneste, Emily Gustafson, Sertac Akar, Charles Morrow, Craig Turchi and Tzahi Cath

Prepared by
Sandia National Laboratories
Albuquerque, New Mexico 87185 and Livermore, California 94550

Sandia National Laboratories is a multi-mission laboratory managed and operated by National Technology & Engineering Solutions of Sandia, LLC, a wholly owned subsidiary of Honeywell International, Inc., for the U.S. Department of Energy's National Nuclear Security Administration under contract DE-NA0003525.

Issued by Sandia National Laboratories, operated for the United States Department of Energy by National Technology & Engineering Solutions of Sandia, LLC.

Available to DOE and DOE contractors from
U.S. Department of Energy
Office of Scientific and Technical Information
P.O. Box 62
Oak Ridge, TN 37831

Telephone: (865) 576-8401
Facsimile: (865) 576-5728
E-Mail: reports@osti.gov
Online ordering: http://www.osti.gov/scitech

Available to the public from
U.S. Department of Commerce
National Technical Information Service
5301 Shawnee Rd
Alexandria, VA 22312

Telephone: (800) 553-6847
Facsimile: (703) 605-6900
E-Mail: orders@ntis.gov
Online order: https://classic.ntis.gov/help/order-methods/

SAND2018-12073
October 19, 2018
Unlimited Release

Multiconfiguration Membrane Distillation Model (MCMD)

Daniel L. Villa
dlvilla@sandia.gov
Energy-Water Systems Integration Department 8825
Sandia National Laboratories
P. O. Box 5800
Albuquerque, New Mexico 87185-1138

Charles Morrow
Advanced Nuclear Fuel Cycle Technology Department 08843

Johan Vanneste, Emily Gustafson, and Tzahi Cath
Colorado School of Mines Civil and Environmental Engineering
vanneste@mines.edu

Craig Turchi, Sertac Akar
National Renewable Energy Laboratory Thermal Systems Research and Development Group
craig.turchi@nrel.gov

Abstract

Many membrane distillation models have been created to simulate the heat and mass exchange process involved but most of the literature only validates models to a couple of cases with minor configuration changes. Tools are needed that allow tradeoffs between many configurations. The multiconfiguration membrane distillation model handles many configurations. This report introduces membrane distillation, provides theory, and presents the work to verify and validate the model against experimental data from Colorado School of Mines and a lower resolution model created at the National Renewable Energy Laboratory. Though more data analysis and testing are needed, an initial look at the model to experimental comparisons indicates that the model correlates to the data well but that design comparisons are likely to be incorrect across a broad range of configurations. More accurate quantification of heat and mass transfer through computational fluid mechanics is suggested. The model is open source software: https://github.com/dlvilla/MCMD1

ACKNOWLEDGMENTS

A special thanks to Charles Morrow and Bryan Dwyer for entrusting me with this work. Also thanks to Charles for mentoring me through this process. This work was funded by the Geothermal Technologies Office of the Department of Energy.

TABLE OF CONTENTS

FIGURES

TABLES

NOMENCLATURE

Symbol	Definition	Units
a_s	Slope of condensate fluid	
c_P	Specific heat of water	J/(kg·K)
C	Mass Transfer coefficient	kg/(m^2·s·Pa)
d_{fs}	Spacer filament diameter	m
d_h	Hydraulic diameter	m
d_{MD}	Mean pore diameter of membrane	m
D	Molecular Diffusivity	
g	Gravitational constant (9.80665)	m/s^2
h	Enthalpy or heat of vaporization/condensation	J/kg
H	Heat transfer coefficient	W/(m^2·K)
k	Thermal conductivity of water	W/(m·K)
K_B	Boltzmann's constant (1.380658E-23)	J/K
K_M	Salinity concentration transfer coefficient	m/s
Kn	Knudsen number $Kn = \frac{\lambda}{d_{MD}}$	
K_s	Spacer correction factor for Nusselt number	
L_g	Length parallel to gravity	m
L_n	Length normal to flow and parallel to plate and frame	m
$\dot{m}$	Mass flow	kg/s
M	Molecular weight (of water unless a subscript added 0.01802)	kg/mol
N	Number of MD layers	
N_h	Number of horizontal control volume divisions	
Nu	Nusselt number $Nu = \frac{Hd_h}{k}$	
N_v	Number of vertical control volume divisions	
P	Total pressure	Pa
Pr	Prandtl number	
P_v	Partial pressure of water vapor in moist air in air gap	Pa
r	Mean pore radius of membrane	m
R	Universal gas constant (8.314)	J/(mol·K)
Ra	Rayleigh number	
Re	Reynold number	
Q	Heat transfer	W
S	Salinity	kg/kg
T	Temperature	K
x	Quality (fraction of condensed water in air/water mixture)	kg/kg
α	Thermal diffusivity	m^2/s
δ	Thickness	m
ε	Porosity	
ϵ	0/1 switch for membrane distillation mass flow	
θ	Spacer filament intersection angle	rad
λ	Mean free path of water vapor molecules	
μ	Dynamic viscosity	Pa·s

Symbol	Definition	Units
a_s	Slope of condensate fluid	
ν	Kinematic viscosity	m^2/s
π	Ratio of a circle's diameter to circumference (3.14159265)	
ρ	Density (of water, air, or air-water mixtures)	
σ	Collisions diameter for water vapor (2.641e-10)	m
τ	Membrane tortuosity (measure of deviation of perfectly cylindrical pores)	
χ	Local control volume coordinate in the gravitational direction	m
Indices		
a	External air	
ab	External air bulk temperature	
AG	Air gap	
avg	Average	
c	Cold-side	
ca	Cold-side ambient	
cb	Cold-side bulk flow	
ci	Cold-side input	
co	Cold-side output	
f	Air gap to condensed fluid interface	
$film$	Indicates a property between bulk and interface in a boundary layer	
fw	Condensed fluid to foil wall interface	
h	Hot-side	
ha	Hot-side ambient	
hb	Hot-side bulk flow	
hi	Hot-side input	
ho	Hot-side output	
i	Insulation	
ia	Interface of insulation to external air	
ic	Interface on the cold side	
ih	Interface on the hot side	
ip	If AGMD $ip = ia$ if DCMD $ip = ic$	
iw	Feed water interface (can be hot or cold side)	
ma	Membrane to air gap interface	
M	Membrane	
MD	Membrane distillation	
p	Membrane distillation type index (*p=AGMD or p=DCMD*)	
ref	Reference	
s	Spacer	
sw	Salt water	
v	Vaporization	
w	Condensed fluid on foil wall	
wb	Cold or hot water feed bulk flow	
wi	Condensed fluid inflow along foil wall	
wo	Condensed fluid outflow along foil wall	

Acronyms

AGMD	Air-gap membrane distillation
CGMD	Conductive gap membrane distillation
CVP	Control volume pair
DAQ	Data acquisition
DCMD	Direct contact membrane distillation
GOR	Gain output ratio
L	Liter
LEP	Liquid entry pressure
LPM	Liters per minute
MD	Membrane distillation
MCMD	Multiconfiguration membrane distillation model
MDHX	Membrane distillation heat exchanger
PFAG	Plate and frame air gap module
PFDC	Plate and frame direct contact
PGMD	Permeate (distillate) gap membrane distillation
ppm	Parts per million
PTFE	polytetrafluoroethylene
PVC	Polyvinyl-chloride
REFPROP	REFerence fluid PROPerties
SGMD	Sweeping gas membrane distillation
SWAG	Spiral wound air gap module
SWDC	Spiral wound direct contact module
VBA	Visual basic for applications
VMD	Vacuum membrane distillation

This page intentionally left blank.

1 INTRODUCTION

Membrane distillation (MD) is a water purification technology created in the 1960's (Bodel, 1963). It has potential for purification of water sources that have low-grade heat (40°C to 80°C) such as geothermal (Orfi et al., 2017; Chandrasekharam et al., 2017; Sarbatly and Chiam, 2013), power plant waste heat (Dow et al., 2016; Khraisheh et al., 2013), and solar power (Ruiz-Aguirre et al., 2015; Zhani et al., 2015). Though fundamental research is improving membrane distillation technology, full scale demonstrations (Mohamed et al., 2017; Chafidz et al., 2014) and market applications (Ashoor et al., 2016, Zhao et al., 2013, Lange et al., 2011) are already underway. The maturity of MD is evident since research includes development of multi-stage systems that maximize heat recovery (Chung et al., 2016) and modularization (Zhao et al., 2013) to make MD economical.

MD uses a hydrophobic membrane to enable water vapor movement across a pressure or concentration difference. Direct contact membrane distillation (DCMD) is the simplest form of MD as seen in Figure 1. The vapor pressure difference proportionally drives water vapor at a rate $\dot{m}_{MD}$. For a successful MD application, the pressure difference across the membrane must not exceed the liquid entry pressure while the membrane porosity, pore radii distribution, and thickness must be tuned to maximize vapor transfer. In addition, the heat transfer should be kept to a minimum to maintain a larger temperature difference, chemical resistance to fouling should be maximized, and sufficient structural strength maintained to integrate the membrane into a working unit. These design issues are addressed more extensively by Deshmukh and Elimelech (2017), González et al. (2017), Ashoor et al. (2016), Wang and Chung (2015), and Alkhudhiri et al. (2012).

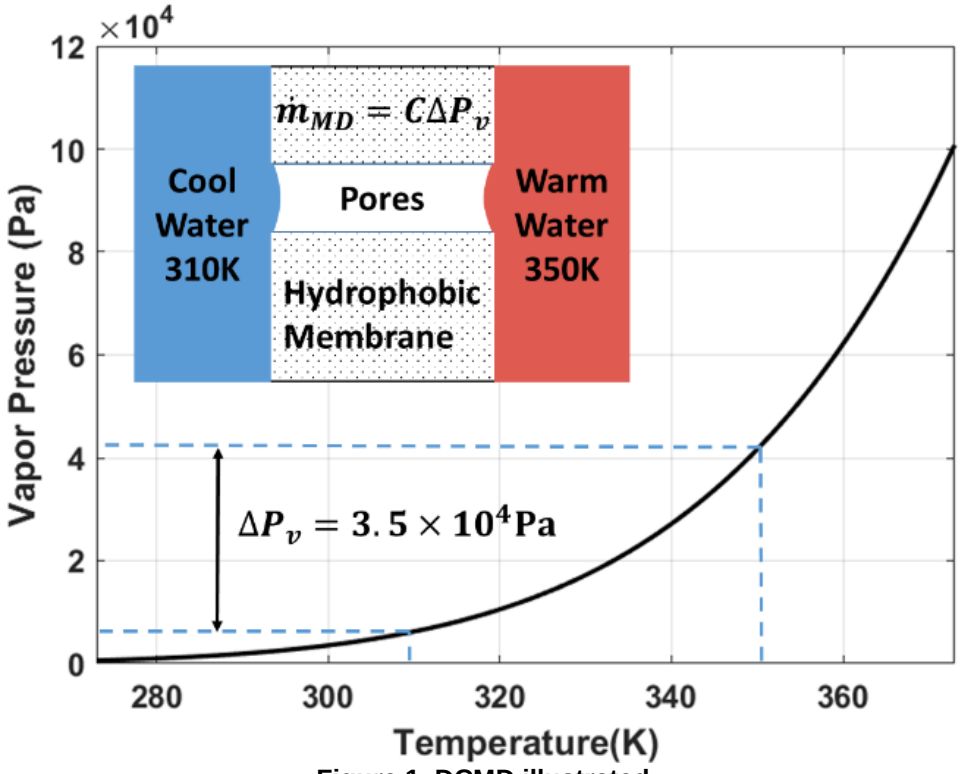

Figure 1. DCMD illustrated.

Many different membrane configurations of single stage MD exist as seen in Figure 2. Beyond DCMD, there is a family of gap membrane distillation configurations. Air gap membrane distillation (AGMD) places a stagnate air gap between the membrane and distillate. This significantly increases the thermal efficiency of the system but also increases the resistance to mass flow. It has the advantage that the distillate is separate from the cool stream. An impermeable foil layer is added that allows heat flow to the cooling stream. Conductive gap membrane distillation (CGMD) uses a permeable material to decrease the thermal resistance across the gap. Permeate (distillate) gap MD (PGMD) seeks to combine the advantages of AGMD and DCMD. Vacuum and sweeping gas membrane distillation (VMD, SGMD) both pump away the distillate to a condenser instead of using a cooling stream directly. Sweeping gas cycles an inert gas whereas vacuum membrane pumps from a dead end. Refer to Eykens et al. (2016) and González et al. (2017) for discussions of the advantages of each configuration.

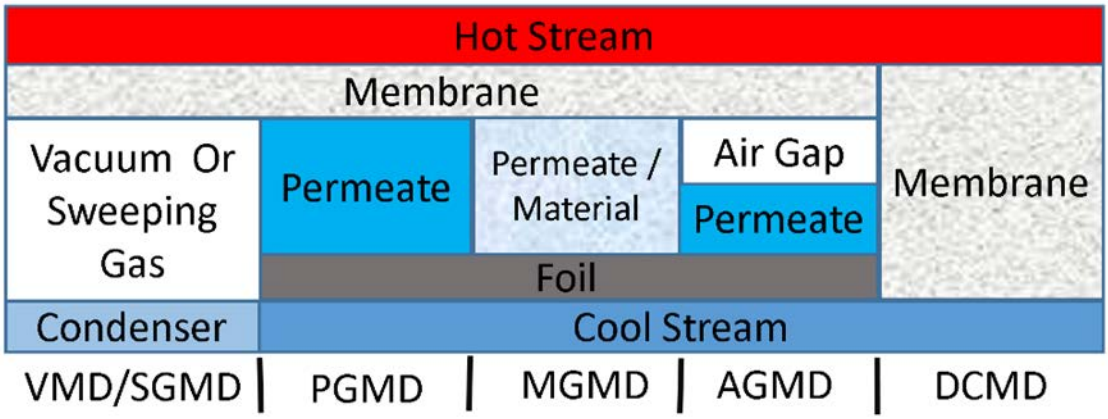

Figure 2. Types of single stage MD.

The literature has shown that the MD heat and mass exchange problem can be accurately solved as a series of one-dimensional, steady state problems (Ashoor et al., 2016, Alkhudhiri et al., 2012) using Nusselt and Sherwood number approximations of the heat and salinity concentration. Even though individual cases fit nicely, the published literature does not provide easy answers concerning whether design comparisons between these types of models produce accurate conclusions (Hitsov et al., 2015). For example, AGMD significantly increases the thermal resistance to conduction of heat through the membrane due to the stagnate air gap. This comes at the cost of a significant barrier to mass flow across the air gap. Whether an air gap is worth including is therefore a complex issue as can clearly be seen in the literature where different studies reach different conclusions (Eykens et al., 2016). Hitsov et al. (2017) produced data that shows AGMD as mildly outperforming DCMD while a more simplified model based assessment by Swaminathan et al. (2016) shows DCMD significantly outperforming AGMD and PGMD. Criscuoli (2016) compares DCMD to a hybrid AGMD-DCMD system and shows improved performance of the hybrid system. Much earlier Alklaibi and Lior (2007) used a 2-D steady flow model that indicated DCMD to have much higher mass fluxes than AGMD. Further research is therefore necessary to delineate whether semi-empirical methods are robust enough to make such comparisons.

The capacity to handle many configurations therefore needs further development such that consistent algorithms are employed when designing MD systems. Designing MD modules needs to be driven toward becoming a common engineering design problem with convenient tools to

make accurate comparisons of MD configurations. To assure this with semi-empirical methods, a considerable amount of data is needed to validate cross-comparisons. To progress toward this goal this effort aims to

1. Propose a framework that allows extension of semi-empirical MD models to many configurations.
2. Show whether such a framework is valid across several configurations at a lab-scale.
3. Propose a software format that allows libraries of configurations, materials, water chemistries, mathematical algorithms, and consistency control measures on these objects.

This paper elaborates on points 1 and 2. Point 3 is critical because it reduces the probability that cross comparisons do not violate known ranges of validity or contain inconsistencies. It has been implemented but is common practice for high quality software development that does not need further discussion.

For the current work, a plate and frame module is assumed. A spiral wound set of data is compared to see if geometry matters. Additional heat exchange terms could extend this to spiral wound, hollow fiber, and other configurations.

This page intentionally left blank.

2 MODELING

This section presents the multi-configuration MD model (MCMD) with a top down approach. First, a general description of the model's kinematics, discretization, and boundary conditions are given. This is followed by a solution procedure that illustrates how new MD configurations can be added. The section is completed by presentation of the physical models used in the analysis in this paper.

2.1 Description

A plate and frame MD model (Villa et al., 2017) was generalized to handle co-flow, counter-flow, cross flow, and any combination of flows that involve full 180 degree turns at the model boundary. All of the flows modeled are one-dimensional, but can have two-dimensional interactions with other one dimensional flows. Reverse of flows is assumed to be symmetric with zero loss in thermal and kinetic energy. Heat flow normal to the mass flow and parallel to the plate and frame is assumed to be zero. Pressure losses due to the flow configurations are not modeled. Three configurations of the model with a 3x3 grid and one layer of hot and cold control volume pairs (CVPs) are shown in Figure 3. Input flow for hot and cold sides can enter any of the four edges of the plate and frame with a specified number of turns for each flow starting from the right or left side. The model is divided vertically and horizontally (N_v, N_h) into CVPs to set the resolution of the calculation. The number of divisions for both dimensions is restricted to be a multiple of the number of flow reversals. This produces a membrane mass exchange area per control volume (A) as follows.

$$A = \frac{L_x L_y}{N_v\, N_h} \tag{1}$$

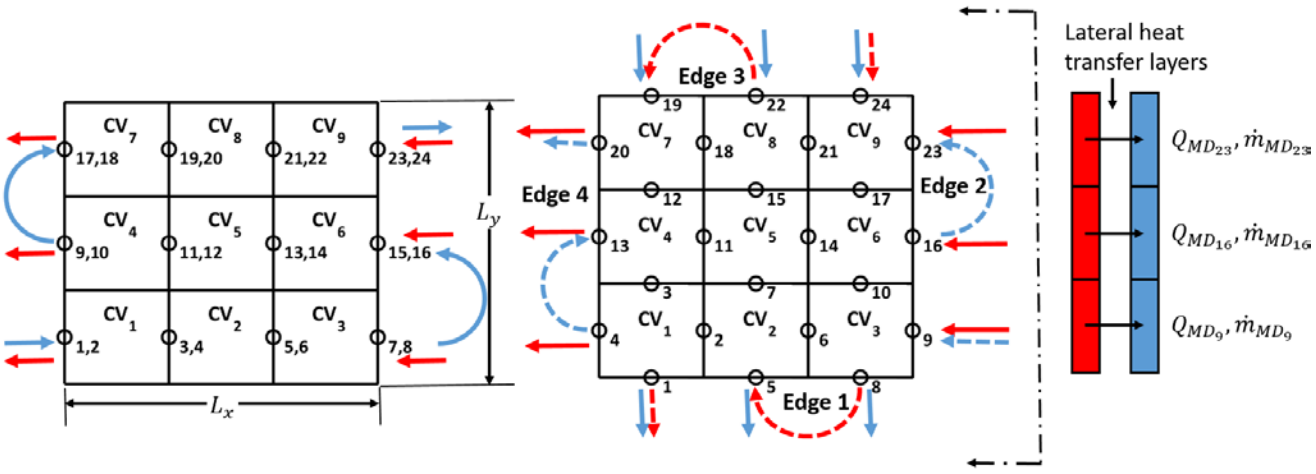

Figure 3. Three model configurations with a single layer of CVPs.

Each CVP has four nodes whose connectivity is governed by working counter-clockwise starting from the bottom edge (Edge 1 in Figure 3) and always counting hot flow nodes first. The control volume numbering starts from the lower left and works to the right and then moves up to the next row. Algorithms were developed to correctly identify the hot and cold inflow and outflow nodes for each CVP such that equations can be applied with no need to track indices in the control

volume equations. The connectivity can be derived from the information provided in the previous sentences but involves complexity that is not elaborated here but can be found in the software algorithms and is presented for a single case in our previous report (Villa et al., 2017).

Boundary conditions for the model include a mixture of input conditions and reversal conditions. Input conditions are enforced by setting the difference between the boundary condition value and the corresponding nodal variable to zero. Reversal conditions are enforced by a symmetric mapping between the flow that assumes unmixed streamlines. Figure 4 shows a mixture of four inflow boundary conditions and two reversal conditions. For the reversal conditions flows, temperatures, and salinities at nodes 8 and 11 are equal to those at nodes 5 and 1.

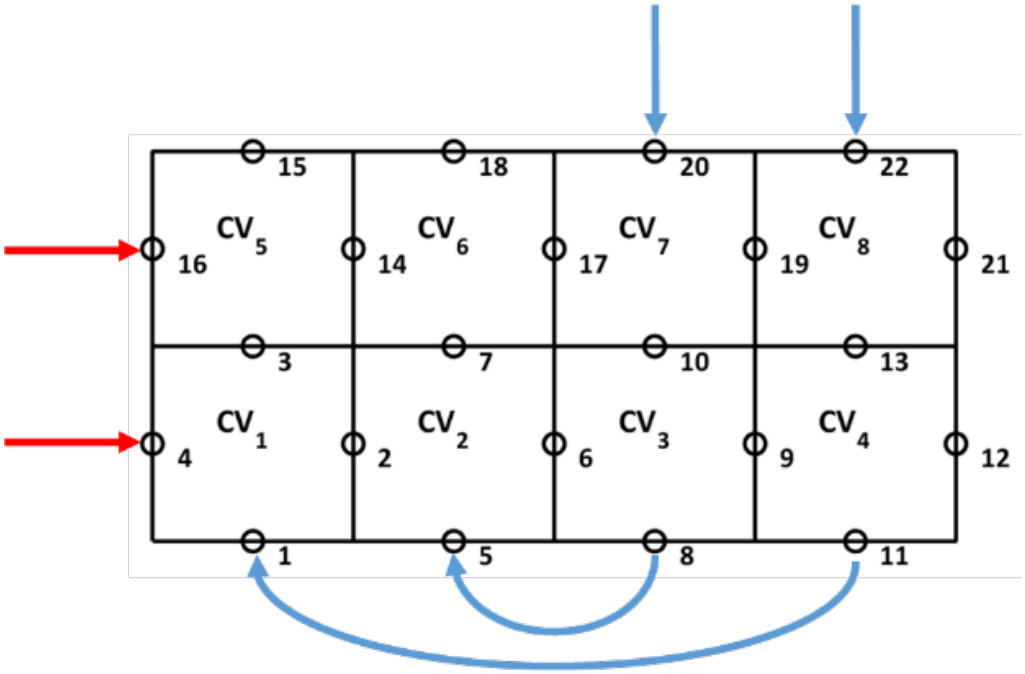

Figure 4. Example boundary conditions.

2.2 Inputs

The inputs to the model are listed in Table 1. Inputs for spacers, water streams, membranes, and foils all access libraries to reduce the number of inputs that are changed whenever the model is reconfigured. This facilitates adding properties to these input objects so that the models representing them can be extended more easily. The current inputs for spacers, water streams, membranes, and foils are shown in Table 2.

Table 1. Model inputs

Input	Explanation	Values/Units
Hot inflow edge	See Figure 3.	1, 2, 3, 4
Hot inflow edge side	This input only makes a difference if there is a hot reversal. When looking normal to the hot inflow edge: 0 = flow starts from the left side, 1 = right side.	0, 1
Hot reversals	Number of times that hot flow reverses. (Restricted by number of divisions)	1 to 100
Cold inflow edge	See Figure 3.	1, 2, 3, 4
Cold inflow edge side	See hot inflow edge side.	0, 1
Cold reversals	See hot reversals.	1 to 100
Horizontal divisions	Number of control volume divisions in the horizontal direction. Horizontal only refers to the model coordinate system.	1 to 100
Vertical divisions	Number of control volume divisions in the vertical direction. Vertical only refers to the model coordinate system.	1 to 100
Cold water stream	Name referring to a water stream library entry.	Only valid names
Cold water spacer	Name referring to a spacer library entry.	Only valid names
Hot water stream	Name referring to a water stream library entry.	Only valid names
Hot water spacer	Name referring to a spacer library entry.	Only valid names
Membrane material	Name referring to a material library entry.	Only valid names
Horizontal Length	Total length of the plate and frame assembly that has active MD mass and heat transfer.	m
Vertical Length	Total vertical length of the plate and frame assembly	
Number of Layers	Number of cold and hot layers that are active. This introduces a multiplication factor. The top and bottom layers can face external losses whereas symmetry is assumed for inner layers.	
MD type	List of types of membrane distillation available. Currently the model only has direct and air gap membrane distillation but the model is designed to be expanded.	Air Gap, Direct Contact
Include ambient losses		True/False
	(If including ambient losses)	
Ambient temperature	Average temperature of the environment surrounding the plate and frame heat exchanger.	°C
External material	Insulation around the plate and frame heat exchanger layers. Name referring to a material library	Only valid names
Side exposed to ambient	Indicates if one or two sides is exposed to ambient	1, 2
	(if only 1 side exposed)	
Is exposed side hot		True/False
	(If air gap MD)	
Foil Material	Wall material between the cold stream and the condensed distillate. Refers to a material library entry.	Only valid names
Air Gap Spacer	Name referring to a spacer library entry	
Gravitational Direction	Direction of gravity in a plane: 1 = up, 2 = left, 3 = down, 4 = right, 5 normal facing out of the plane, and 6 normal facing into the plane	1,2,3,4,5,6

Table 2. Inputs for interchangeable libraries

Input	Spacer	Membrane	Foil	Water Stream
1	Thickness[1]	Thickness[1]	Thickness[1]	Temperature[7]
2	Filament diameter[1]	Thermal conductivity[2]	Thermal conductivity[2]	Volume flow rate[5]
3	Filament intersection angle[4]	Direct input of mass transfer coefficient (true/false)		Salinity[6]
4	Porosity	Direct mass transfer coefficient[3]		
5	Thermal conductivity[2]	Porosity		
6		Mean pore radius[1]		

[1] mm, [2] W/(m·K), [3] kg/s/m^2/Pa, [4] ° (angular), [5] LPM, [6] g/kg, [7] °C

2.3 Solution Procedure

The solution procedure decouples the physics and the mathematical solution of nonlinear equations to enable the use of an arbitrary mathematical solver. To reduce the total number of variables in the solution, a hybrid approach was developed that solves the global mass, salinity, and energy equations and then solves a smaller set of equations for lateral heat and mass transfer between individual CVPs Q_{MD}, Q_{ha}, Q_{ca} and $\dot{m}_{MD}$. For each CVP, the global equations are formulated by balancing mass and energy as seen in the following equations:

$$\dot{m}_{hi}c_P(T_{hi},S_{hi})\left(T_{hi}-T_{ref}\right)-\dot{m}_{ho}c_P(T_{ho},S_{ho})\left(T_{ho}-T_{ref}\right)-Q_{MD}-Q_{ha}=0 \quad (2)$$

$$\dot{m}_{ci}c_P(T_{ci},S_{ci})\left(T_{ci}-T_{ref}\right)-\dot{m}_{co}c_P(T_{co},S_{co})\left(T_{co}-T_{ref}\right)+Q_{MD}-Q_{ca}=0 \quad (3)$$

$$\dot{m}_{hi}-\dot{m}_{ho}-\dot{m}_{MD}=0 \quad (4)$$

$$\dot{m}_{ci}-\dot{m}_{co}+\epsilon_p\dot{m}_{MD}=0 \quad (5)$$

$$\dot{m}_{hi}S_{hi}-\dot{m}_{ho}S_{ho}=0 \quad (6)$$

$$\dot{m}_{ci}S_{ci}-\dot{m}_{co}S_{co}=0 \quad (7)$$

$$\epsilon_p=\begin{cases}1 & p\equiv DCMD\\ 0 & p\equiv AGMD\end{cases} \quad (8)$$

Here $\dot{m}_{hi}$, $\dot{m}_{ho}$, $\dot{m}_{ci}$, $\dot{m}_{co}$ are the hot input, hot output, cold input, and cold output mass flows for the current control volume; T_{hi}, T_{ho}, T_{ci}, and T_{co} are the corresponding temperatures; and S_{hi}, S_{ho}, S_{ci}, and S_{co} are the corresponding salinities. c_P is the specific heat of water as a function of temperature and salinity. c_P and all other thermal properties are provided in Appendix A Table 9. Q_{MD}, Q_{ha}, and Q_{ca} are the MD, hot ambient loss, and cold ambient loss heat transfers. The ambient losses are set to zero unless the user specifies for external losses to be included. T_{ref} is the reference temperature for the specific heat function equal to 273.15K. Equations (2) to (7) are applied to the number of CVPs for a total of $6N_vN_h$ equations. In addition to this, the temperature, inflow, and salinity boundary conditions total $3N_v+3N_h$. These two numbers sum to the number of nodal variables (temperature, flow, salinity) producing a balanced system of nonlinear equations.

The global equations presented thus far can include many different MD configurations through different models for the lateral mass and heat transfers $\dot{m}_{MD}$ and Q_{MD}. For the first solution of the global equations, guesses for the lateral heat flow, Q_{MD}, are made for the CVPs by assuming a fraction of the maximum possible heat transfer. The lateral mass transfer, $\dot{m}_{MD}$, is initially assumed to be a very small fraction of the overall input flow. The global equations can then be solved for nodal temperatures starting from an assumed linear change from input to output along the flow path. With these values set, the lateral heat and mass flow for each CVP can be solved. The average bulk flow temperatures of the hot side and cold flows T_{hb} and T_{cb} are assumed to be the average of the input and output flows.

$$T_{hb}=\frac{T_{hi}+T_{ho}}{2} \quad (9)$$

$$T_{cb} = \frac{T_{ci} + T_{co}}{2} \tag{10}$$

The same is assumed for mass and salinity. The bulk flow variables (T_{cb}, T_{hb}) and the external air temperature (T_{ab}) are held fixed while the set of independent variables for lateral heat and mass transfer, X, for AGMD or DCMD shown in Figure 5 are found through solving the equations in Table 3 with a nonlinear solver for each control volume. The equations in Table 3 are balances that equate heat or mass transfers across different layers assuming steady state operation of the MD unit. The external losses variables are shown in the right-hand side of Figure 6.

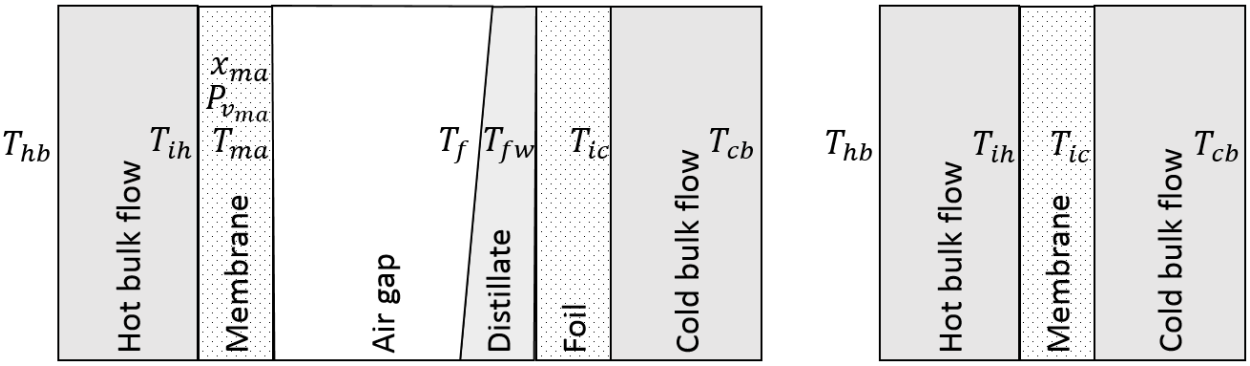

Figure 5. Lateral heat transfer variables for AGMD (left) and DCMD (right). Note that T_{hb} and T_{cb} are variables that are calculated for the global equation set. They are fixed when each CVP's lateral heat and mass transfer are being calculated.

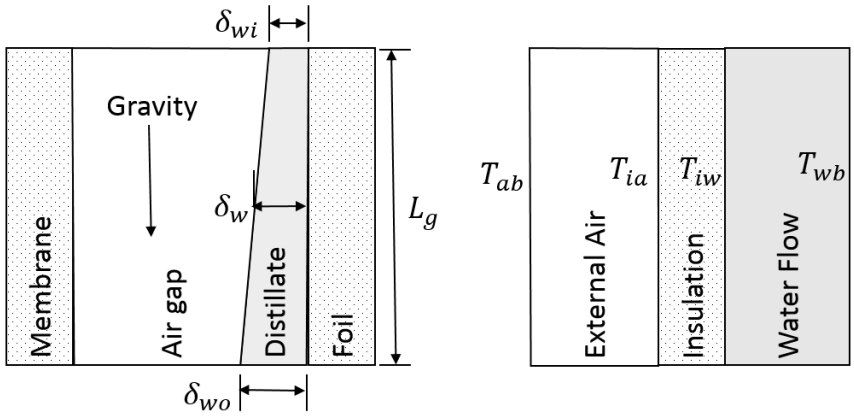

Figure 6. (left) Distillate dependent variables(right) external losses variables (gravity may not be parallel to the hot and cold stream flows).

Table 3. Lateral heat transfer equations for DCMD and AGMD and for external losses

	DCMD ($\dot{m}_{MD}$, Q_{MD})	AGMD ($\dot{m}_{MD}$, Q_{MD})	External losses (Q_{ha}, Q_{ca})
1	$H_h(T_{hb} - T_{ih})$	$H_h(T_{hb} - T_{ih}) - H_{MD}(T_{ih} - T_{ma}) = 0$	$H_a(T_{ia} - T_{ab})$
	$-H_{MD}(T_{ih} - T_{ic}) = 0$		$-H_i(T_{iw} - T_{ia}) = 0$
2	$H_{MD}(T_{ih} - T_{ic})$	$H_{MD}(T_{ih} - T_{ma}) - H_{AG}(T_{ma} - T_f) = 0$	$H_{iw}(T_{wb} - T_{iw})$
	$-H_c(T_{ic} - T_{cb}) = 0$		$-H_i(T_{iw} - T_{ia}) = 0$
3		$H_{AG}(T_{ma} - T_f) - H_f(T_f - T_{fw}) = 0$	
4		$H_f(T_f - T_{fw}) - H_w(T_{fw} - T_{ic}) = 0$	
5		$H_w(T_{fw} - T_{ic}) - H_c(T_{ic} - T_{cb}) = 0$	
6		$\dot{m}_{MD} - \dot{m}_{AG} = 0$	
7		$\delta_w - \frac{\delta_{wi} + \delta_{wo}}{2} = 0$	
$\boldsymbol{X}$	$\{\boldsymbol{T_{ih}}, \boldsymbol{T_{ic}}\}$	$\{\boldsymbol{T_{ih}}, \boldsymbol{T_{ma}}, \boldsymbol{T_f}, \boldsymbol{T_{fw}}, \boldsymbol{\delta_w}, \boldsymbol{P_{v_{ma}}}/(\mathbf{1} + \boldsymbol{x_{ma}})\}$	$\{\boldsymbol{T_{iw}}, \boldsymbol{T_{ia}}\}$

$H_h, H_{MD}, H_{AG}, H_f, H_w, H_c, H_a, H_i, H_{iw}$ are the heat transfer coefficients on the hot side due to convection, through the membrane due to evaporation and heat conduction, through the air gap due to conduction and condensation, through the condensed fluid due to conduction, through the foil wall due to conduction, on the cold side due to convection, external losses due to natural convection, external losses through insulation due to conduction and external losses due to forced convection from the hot or cold feed. The temperatures, T, are illustrated in Figure 5 and Figure 6. The distillate thicknesses are defined in Figure 6. $\dot{m}_{AG}$ is the mass flux across the air gap, $P_{v_{ma}}$ is the partial pressure of water vapor at the membrane air gap interface, and $x_{ma}$is the quality of water at the membrane air gap interface. Only one of $P_{v_{ma}}$and $x_{ma}$is an independent variable. $\delta_w$is the average thickness of condensed fluid in the gravitational direction. It is calculated as a function of T_f and T_{ma}, δ_{wi} and δ_{wo} are the input and output condensate fluid thicknesses. A linear model for condensate thickness is assumed for each control volume.

For AGMD, the distillate is assumed to equilibrate with the cold stream before flowing in the gravitational direction. This assumption avoids another mass and heat balance for the distillate stream in the global equations. The distillate thickness variables shown on the left-hand side of Figure 6 are not independent but require specification of the gravitational direction which can be any in-plane direction. Unlike DCMD, the vapor pressure exiting the membrane may not be the saturated vapor pressure. The seventh AGMD variable, X_7, is therefore a combination of the vapor pressure at the air gap/membrane interface ($P_{v_{ma}}$) and the quality of water at that interface (x_{ma}). This composite variable handles a thermodynamic transition between true AGMD and cases where the air gap contains condensed water droplets smoothly. While AGMD is dominating $P_{v_{ma}}$varies as a value less than the saturated vapor pressure of water for the air gap temperature ($P_{sat}(T_{ma})$) but x_{ma} remains equal to 1. If the solver suggests a value of X_7 that is greater than $P_{sat}(T_{ma})$ allows, $P_{v_{ma}}$ is set equal to $P_{sat}(T_{ma})$ while x_{ma} reduces from 1 toward zero.

$$x_{ma} = \begin{cases} \frac{P_{sat}(T_{ma})}{X_7} - 1 & X_7 > P_{sat}(T_{ma})/2 \\ 1 & X_7 \leq P_{sat}(T_{ma})/2 \end{cases} \quad (11)$$

$$P_{v_{ma}} = \begin{cases} P_{sat}(T_{ma}) & X_7 > P_{sat}(T_{ma})/2 \\ 2X_7 & X_7 \leq P_{sat}(T_{ma})/2 \end{cases} \quad (12)$$

This arrangement has served to stabilize the numerical search much more robustly than applying a hard constraint for AGMD ($P_{v_{ma}} \leq P_{sat}(T_{ma})$).

Once the relevant independent variables have been found, the lateral mass and heat transfers Q_{MD}, Q_{ha}, Q_{ca}, and $\dot{m}_{MD}$ can be recalculated and the global equation set resolved. An iterative loop is repeated until a convergence criterion is satisfied for the global solver. As arranged, this solution procedure makes it straightforward to add a new column to Table 3 so that any number of membrane distillation configurations can be modeled without having to rework any other portion of the model.

2.4 Membrane Distillation Models

The multiconfiguration MD model contains models for heat transfer, mass transfer, and salinity concentration. These models require constitutive relationships for physical properties that are provided in Appendix A Table 7.

2.4.1 Heat Transfer

The modeling requires a mixture of heat transfer coefficients including conduction, forced convection in the feed channels, and natural convection of air for external losses. Mass transfer across the membrane also moves energy through phase transitions. When calculating dimensionless numbers, the length scale must be close to the relevant overall plate and frame length in order to avoid scaling the heat transfer with the model discretization. This portion of the model is semi-empirical because even though the relationships are non-dimensional, their validity is centered on the size scale, geometry, and flow regime of the measurements involved.

2.4.1.1 Forced Convection

The assumptions of Alsaadi et al. (2013) were used to calculate the Nusselt number with parameters included for the spacers. Even though Reynolds' numbers for the channel are in the laminar region (<300), a fully turbulent flow over a flat surface Nusselt relationship is used because it fits the experimental data for this study and for that of Alsaadi et al. (2013) and Zhang et al. (2012) well. Both the hot and cold flows use the same relationships to determine H_h, H_c, and H_{iw}.

$$H = \frac{Nu\ k}{d_h} \quad (13)$$

$$Nu = 0.029 K_s Re^{0.8} Pr^{0.33} \quad (14)$$

$$K_s = 1.904\left(\frac{d_{fs}}{\delta_s}\right)^{-0.039} \varepsilon_s^{0.75}\left[sin\left(\frac{\theta}{2}\right)\right]^{0.086} \quad (15)$$

$$Re = \frac{\dot{m} d_h}{\mu \delta_s L_n} \quad (16)$$

$$Pr = \frac{c_P \mu}{k} \quad (17)$$

$$d_h = \frac{4\varepsilon_s d_{fs} \delta_s}{2d_{fs} + 4(1-\varepsilon_s)\delta_s} \quad (18)$$

Here H is a heat transfer coefficient due to forced convection, k is the thermal conductivity of water as a function of temperature and salinity, d_h is the hydraulic diameter, Nu is the Nusselt number, K_s is a spacer correction factor, Re is the Reynolds number, Pr is the Prandtl number, d_{fs} is the spacer filament diameter, δ_s is the spacer thickness, ε_s is the spacer porosity, θ is the spacer filament intersection angle, $\dot{m}$ is mass flow for the current channel and control volume, μ is the dynamic viscosity of water as a function of temperature and salinity, and L_n is the length normal to flow and parallel to the plate and frame.

2.4.1.2 Natural Convection

External losses are insignificant for multi-layer MD units (~0.1-0.4%) but become more important for lab-scale single layer units (1-4%). A model of external, natural convection that assumes a vertical plate and frame with uniform wall temperature (London, 2000) is used to determine H_a by equation (13). The Reynolds number is replaced with Rayleigh number (Ra) since air movement is unforced.

$$Nu = \begin{cases} 0.68 + \dfrac{0.670Ra^{1/4}}{[1+(0.492/Pr_a)^{9/16}]^{4/9}} & 10^5 < Ra < 10^9 \\ \left[0.825 + \dfrac{0.387Ra^{1/6}}{[1+(0.492/Pr_a)^{9/16}]^{8/27}}\right]^2 & 10^9 < Ra < 10^{12} \end{cases} \quad (19)$$

$$Ra = \frac{g\beta_a |T_{ia} - T_{ab}| L_g^3}{\alpha_a \nu_a} \quad (20)$$

Here g is the gravitational constant (~9.81m/s^2) and β_a is the thermal expansion coefficient for air. L_g is the length parallel to gravity for the plate and frame assembly, α_a is the thermal diffusivity of dry air as a function of temperature, ν_a is the kinematic viscosity of dry air as a function of temperature, and Pr_a is the Prandtl number of dry air as a function of temperature calculated as an empirical function in Table 9. The effects of humidity in the external air are neglected. Assuming an ideal gas, $\beta_a = 1/T_{film}$ where $T_{film} = (T_{ia} + T_{ab})/2$. All dry air thermal properties are evaluated at T_{film}.

2.4.1.3 Conduction and Phase Change

The remaining heat transfer coefficients are either simple conduction or a mixture of conduction and phase change. The heat transfer across condensate (H_f), Foil wall (H_w), and external insulation (H_i) are all assumed to be dominated by conduction.

$$H = \frac{k}{\delta} \tag{21}$$

Here k is the thermal conductivity of the relevant material and δ is the material thickness. The membrane heat transfer coefficient involves both conduction and the heat of vaporization.

$$H_{MD} = \frac{k_{MD}}{\delta_{MD}} + \frac{\dot{m}_{MD} h_v x_{mp}}{\delta_s L_n \left(T_{ih} - T_{ip}\right)} \tag{22}$$

$$x_{mp} = \begin{cases} 1 & p \equiv DCMD \\ x_{ma} & p \equiv AGMD \end{cases} \tag{23}$$

$$T_{ip} = \begin{cases} T_{ic} & p \equiv DCMD \\ T_{ma} & p \equiv AGMD \end{cases} \tag{24}$$

Here k_{MD} is the effective membrane thermal conductivity, δ_{MD} is the membrane thickness, h_v is the heat of vaporization of water as a function of temperature, and x_{mp} is the quality of water exiting the membrane. T_{ip} is the air to membrane interface temperature (T_{ma}) for AGMD or the cold channel interface temperature (T_{ic}) for DCMD. The effective membrane thermal conductivity is calculated through a Maxwell type I equation used by Hitsov et al. (2015).

$$k_{MD} = k_a \frac{1 + 2\xi(1 - \varepsilon_{MD})}{1 - \xi(1 - \varepsilon_{MD})} \tag{25}$$

$$\xi = \frac{k_M - k_a}{k_M + 2k_a} \tag{26}$$

Here k_a is the thermal conductivity of air as a function of temperature. k_M is the thermal conductivity of the membrane material with zero porosity and ε_{MD} is the membrane porosity. The thermal properties k_a and h_v are evaluated at the average temperature in the membrane ($\left(T_{ih} + T_{ip}\right)/2$) and k_M is assumed to be a constant value. Finally, the air gap heat transfer coefficient is H_{AG} needed if AGMD is selected.

$$H_{AG} = \frac{k_{av}\varepsilon_s + k_s(1 - \varepsilon_s)}{\delta_s} + \frac{\dot{m}_{MD}\left(h_{va} - h_f\right)}{\delta_s L_n \left(T_{ma} - T_f\right)} \tag{27}$$

Here k_{av} is the thermal conductivity of a saturated air water mixture. Because of the low pressures involved, a saturated air-water mixture is assumed. k_s is the thermal conductivity of the spacer, h_{va} is the enthalpy of humid air and condensed water entering the air gap and h_f is the enthalpy of saturated liquid water exiting the air gap at T_f. The enthalpies are evaluated at

T_{ma} and T_f. k_{av} is evaluated at the average temperature in the air gap ($(T_{ma} + T_f)/2$) and the air gap pressure P_{AG}. h_{va} is a function of the enthalpy of saturated water vapor h_{wv} and of saturated liquid water h_{wl} at T_{ma} and x_{ma}.

$$h_{va} = h_{wv}(T_{ma},)x_{ma} + h_{wl}(T_{ma})(1 - x_{ma}) \quad (28)$$

2.4.2 Mass Transfer

2.4.2.1 Membrane

The mass transfer for MD can be written as proportional to the change in vapor pressure across the membrane.

$$\dot{m}_{MD} = C_{MD} A \left(P_{sat}(T_{ih}) - P_{v_p} \right) \quad (29)$$

$$P_{v_p} = \begin{cases} P_{sat}(T_{ic}) & p \equiv DCMD \\ P_{v_{ma}} & p \equiv AGMD \end{cases} \quad (30)$$

The membrane mass transfer coefficient (C_{MD}) model follows the Knudsen model presented by Khayet (2011) with an assumed uniform pore radius (r). The relationships are affirmed by Khayet for DCMD but are shown in this study to produce good results for AGMD as well. The mass transfer coefficient (C) transitions between flow mechanisms with the Knudsen number (Kn). For $Kn > 1$ Knudsen flow dominates; $0.01 < Kn < 1$ marks a transition between Knudsen flow and molecular diffusion; and $Kn < 0.01$ is dominated by molecular diffusion (Khayet, 2011).

$$C_{MD} = \begin{cases} \frac{2\varepsilon_{MD} r}{3\tau\delta_{MD}} \sqrt{\frac{8M}{\pi RT}} & Kn > 1 \\ \frac{M}{RT\delta_{MD}} \left(\frac{3\tau}{2\varepsilon_{MD} r} \sqrt{\frac{\pi M}{8RT}} + \frac{P_a \tau}{\varepsilon_{MD} PD} \right)^{-1} & 0.01 < Kn < 1 \\ \frac{\pi}{RT} \frac{PD}{P_a} \frac{r^2}{\tau\delta_{MD}} & Kn < 0.01 \end{cases} \quad (31)$$

Here M is the molecular weight of water (.01802kg/mol), τ is the tortuosity, δ_{MD} is the membrane thickness, R is the universal gas constant (8.314 J/(mol·K)), T is the average temperature in the membrane, P is the total pressure in the membrane pores, D is the mass diffusivity between the air and water vapor, and P_a is the partial pressure of air in the membrane pores. Several additional relationships specify the various terms in this equation. The Knudsen number is the ratio of the mean free path of water vapor (λ) and the mean pore diameter.

$$Kn = \frac{\lambda}{2r} \quad (32)$$

$$\lambda = \frac{K_B T}{\sqrt{2}\pi P \sigma^2} \quad (33)$$

Here, K_B is Boltzmann's constant (1.380658E-23 J/K) and σ is the collision diameter for water vapor (2.641e-10m). The total pressure times the mass diffusivity between air and water vapor (PD) and the tortuosity (τ) as a function of membrane porosity were empirically fit by Alkhudhiri et al. (2012).

$$PD = 1.895 \times 10^{-5} T^{2.072} \quad (34)$$

$$\tau = \frac{(2-\varepsilon_{MD})^2}{\varepsilon_{MD}} \quad (35)$$

2.4.2.2 Air Gap

All properties in the air gap are evaluated at the average temperature between the independent variables T_{ma} and T_f.

$$T_{AG} = \frac{T_{ma}+T_f}{2} \quad (36)$$

The resistance to mass transfer across the air gap follows the formulation of Alsaadi et al. (2013). Once again, mass transfers due to a vapor pressure gradient as the water air mixture cools across the gap.

$$\dot{m}_{AG} = C_{AG} A \left(P_{v_{ma}} - P_{sat}(T_f) \right) \quad (37)$$

The gap mass transfer coefficient was taken to be the same as that of Hitsov et al. (2017). This model assumes a stagnant air gap binary diffusion of vapor and air.

$$C_{AG} = \frac{D_{AG} M_{av}}{(\delta_s - \delta_w) T_{AG} R} ln\left(\frac{P_{AG} - P_{sat}(T_f)}{P_{AG} - P_{v_{ma}}} \right) \frac{1}{P_{v_{ma}} - P_{sat}(T_f)} \quad (38)$$

Here δ_w is the thickness of the condensate, M_{av} is the molecular weight of the air-water mixture at the average temperature in the air gap, and P_{AG} is the total pressure in the air gap. D_{AG} is the diffusivity of the air water mixture as defines by Hitsov et al. (2017).

$$M_{av} = \left(\frac{P_{v_{ma}} + P_{sat}(T_f)}{2P_{AG}} \right) M_v + \left(1 - \left(\frac{P_{v_{ma}} + P_{sat}(T_f)}{2P_{AG}} \right) \right) M_a \quad (39)$$

$$D_{AG} = 4.46e\text{-}6 T_{AG}^{2.334} \quad (40)$$

δ_w is an independent variable that is balanced with Nusselt film condensation on a vertical plate (Asaadi et al., 2013).

$$\frac{\dot{m}_{AG}}{A} = \frac{\rho_f(\rho_f - \rho_{AG})g\delta^2}{\mu_f}\frac{d\delta}{d\chi} \tag{41}$$

Here ρ and μ are the density and dynamic viscosity of condensed water at the average temperature in the condensed fluid. χ is a local coordinate in the gravitational direction varying from 0 to L_g; δ is the condensate fluid thickness as a function of χ; and ρ_{AG} is the air-water mixture density at T_{AG}. Assuming an ideal gas mixture leads to the following expression.

$$\rho_{AG} = \frac{P_{AG}M_{av}}{RT_{AG}} \tag{42}$$

To estimate δ, a linear form is assumed and $\dot{m}_{AG}$ is assumed to be uniform along the length. When solved from top to bottom (w/r to the gravitational direction), the last control volume's exit condensate thickness, δ_{wi}, is known. This immediately provides the intercept of the linear profile at $\chi = 0$. With the slope of condensate fluid designated as a_s, the equation is written as follows.

$$\frac{\dot{m}_{AG}}{A} = \frac{\rho(\rho - \rho_{AG})g(a_s\chi + \delta_{wi})^2}{\mu}\frac{d(a_s\chi + \delta_{wi})}{d\chi} \tag{43}$$

Simplifying this expression and evaluating at L_g produces a_s as a third order polynomial. This 1st order collocation solution of the differential equation keeps the end points as solutions with linear segments between them.

$$L_g^2 a_s^3 + 2L_g\delta_{wi}a_s^2 + \delta_{wi}^2 a_s - \frac{\dot{m}_{AG}\mu}{A\rho_f(\rho_f - \rho_{AG})g} = 0 \tag{44}$$

Finding the smallest, real, positive root to this equation for a_s enables calculation of δ_{wo}.

$$\delta_{wo} = a_s L_g + \delta_{wi} \tag{45}$$

2.4.3 Salinity Concentration

For both DCMD and AGMD, the hot feed will have concentrated salinity at the feed to membrane interface due to the viscous boundary layer. The membrane mass flow ($\dot{m}_{MD}$) also increases salinity concentration by only allowing pure water through the membrane. Though this is much weaker than thermal effects (Martínez-Díez and Vázquez-González, 1999), it is included for completeness. The formulation of Hitsov et al. (2015) is followed.

$$S_i = S_{avg} e^{\frac{\dot{m}_{MD} M_{sw}}{A M \rho K_M}} \quad (46)$$

$$S_{avg} = \frac{S_{hi} + S_{ho}}{2} \quad (47)$$

$$K_M = \frac{Sh D_{sw}}{d_h} \quad (48)$$

$$Sh = 1.86 \left(\frac{Re Sc d_h}{L_n} \right)^{0.33} \quad (49)$$

$$Sc = \frac{\mu}{\rho D_{sw}} \quad (50)$$

$$M_{sw} = M\left(1 - S_{avg}\right) + M_{NaCl} S_{avg} \quad (51)$$

Here S_i is the interface salinity (hot or cold side), S_{avg} is the average bulk flow salinity for the hot current control volume, M_{sw} is the molecular weight of the saline bulk flow, K_M is the mass transfer coefficient, Sh is the Sherwood number which is the mass transfer analogy to heat transfer's Nusselt number, Sc is the Schmidt number, and D_{sw} is the solute diffusivity which is calculated according to the Nernst-Haskell equation passed on by Chiam and Sarbatly (2016) as defined in Table 9.

2.5 Multiple layers

When more than one layer is specified in the model, it is assumed that there is symmetry at the mid-point of each hot and cold stream as seen in Figure 7. If more than 1 layer is selected, then 3 simulations are required to account for the asymmetry of the insulation. More than one layer requires a multiplying factor over the heat and mass transfer plus different heat and mass transfers for the outer layers. $Q_{hot}, \dot{m}_{MD_{hot}}, Q_{cold}$ and $\dot{m}_{MD_{hot}}$. For the symmetrical cases, the global mass flows are multiplied by ½. For the boundary cases the hot or cold flow next to the insulation is multiplied by 1 while the flow on the other side is multiplied by ½.

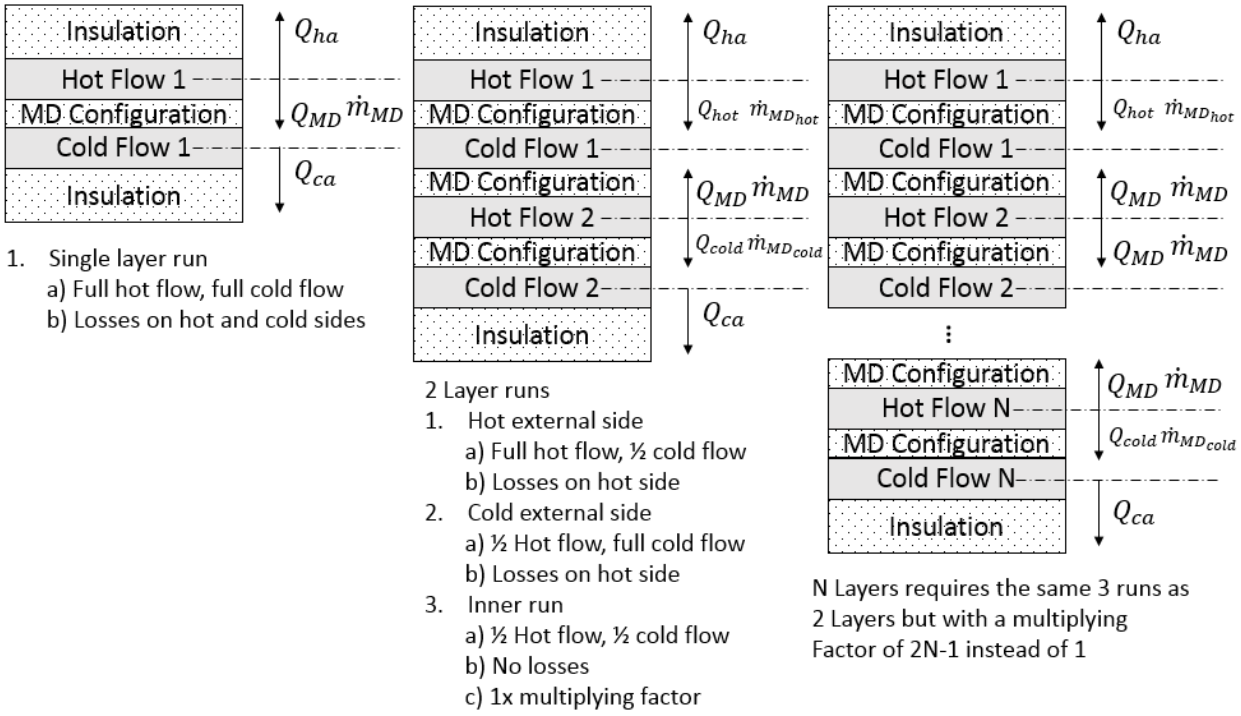

Figure 7. Layer model.

3 EXPERIMENTAL SETUP

Experimental validation of the MCMD model was performed using 73 tests on 6 configurations More tests were conducted but an error invalidated the results. The configurations provide comparative data between plate and frame versus spiral wound modules, membrane type, feed and distillate input temperatures, number of layers, flow rate, and counter-flow versus co-flow. The question of the model's sensitivity to changes in configuration versus the experimental sensitivity moves validation beyond fitting a semi-empirical model to a single configuration toward evaluating whether the semi-empirical methods prevalent in MD modeling can be used to compare different configurations for design purposes.

3.1 Solution chemistry

Experiments were performed with a synthetic solution of American Chemical Society grade NaCl at 4000ppm as the hot feed stream and deionized water as the cold stream (distillate stream for DCMD).

3.2 Membranes

Three hydrophobic, microporous membranes were tested in this study. These include membranes from CLARCOR (QL822, Franklin, TN), 3M (0.2 micron, Maplewood, MN), and Aquastill (0.3 micron, Sittard, Netherlands). CLARCOR is an asymmetric membrane, made from polytetrafluoroethylene (ePTFE) with a polypropylene support material. It has a mean pore diameter of 0.45 µm, porosity of 70-85% with a porosity of 75% used in this study, and a thickness of 127-203 µm. An active thickness of 50µm is assumed in this study. 3M and Aquastill are both isotropic membranes, each with a porosity of 85%. 3M is made from polypropylene, has a mean pore diameter of 0.59 µm, and a thickness of 110 µm. Aquastill is made from polyethylene, has a mean pore diameter of 0.3 µm, and a thickness of 75 µm. The model is not significantly sensitive to thermal conductivity at the high porosities of the membranes. Nominal values of the bulk membrane materials are therefore sufficient.

3.3 Module configurations

Four configurations of three different modules were used in the experiments: plate and frame air gap (PFAG), plate and frame direct contact (PFDC), spiral wound air gap (SWAG), and spiral wound direct contact (SWDC). Module 1 is a custom-made plate and frame designed for multiple configurations including DCMD, AGMD, and MD Heat Exchanger (MDHX). Channels in module 1 consist of nitrile gaskets with a rectangular cutout while the module material itself is made from 2.54cm thick Delrin 150. Modules 2 and 3 were flat-sheet membranes spiral wound by Aquastill with 18 parallel membrane layers. Module 2 is configured for SWDC and Module 3 for SWAG. DelStar Technologies Inc. (Austin, TX) diamond mesh spacers (Product number 113796-0) with 2mm thickness, were used on each side of the membrane in both the feed and distillate channels of all three modules. The spacers are polypropylene with a filament diameter of 0.9mm, a mesh size of 4.23mm and a hydrodynamic angle of 60°. The physical dimensions of the modules' channels are summarized in Table 4. The effective width of the membrane for the plate and frame module was 25.4mm less than the channel width. A complete list of materials and properties are listed in Table 5.

Table 4. Channel dimensions of the three modules used in experiments

Module	Flow channel length l (m)	Flow channel width w (m)	Flow channel height h (m)	Number of layers (-)	Membrane surface area (m^2)
1 (PFDC/PFAG)	1.04	0.2476 (0.2222)[1] (0.135)[2]	0.002	1 or 2	0.231
2 (SWDC)	0.5	0.4	0.002	9	3.6
3 (SWAG)	3.8	0.4	0.002	9	27.4

[1] This is the effective width of the membrane. [2] The air gap runs have gravity normal to the flow chamber when tilted vertical.

Table 5. Constant material properties

Description	Material	Thickness (mm)	Thermal Conductivity (W/(m*K))	Porosity (%)	Mean Pore Diameter (µm)	Filament Intersect Angle (°)	Filament Diameter (mm)
CLARCOR QL822 Module 1	Polytetrafluoroethylene	0.050	0.27	75	0.45		
Housing	DELRIN 150	25.4	0.37				
Air Gap Foil	Stainless Steel 304	0.1778	15.1				
Aquastill	Polyethylene	0.075	0.4	85	0.30		
3M	Polypropylene	0.11	0.15	85	0.59		
Delstar Spacer	Polypropylene	2	0.15	92		60	0.9

3.4 Pilot scale system description

Pilot scale tests were performed to determine water flux (mass flow), and heat flows. The MD system was connected to LabVIEW (National Instruments, Austin, TX) software on a Windows PC using a data acquisition (DAQ) device (Model UE9-Pro**,** LabJack Corporation, Lakewood, CO**)** for system control and DAQ.

Three heat exchangers in the MD system provided both heating and cooling to the feed and distillate streams. A detailed flow schematic of the experimental setup is provided in Figure 8. For module 1, a 28L cylindrical clear polyvinyl-chloride (PVC) feed tank and a 16L cylindrical clear PVC distillate tank were connected to “low flow” (< 4 L/min) positive displacement gear pumps (Micropump Integral Series, IDEX Corp. Vancouver, Washington) that circulated each stream through a “preheater” heat exchanger to remove the heat from the distillate and return it to the feed. The feed flow continued through an additional “heater” heat exchanger, which controlled the temperature by adjusting the flow of hot water provided by the building, before entering the module. The distillate circulated through a third “cooler” heat exchanger, which was supplied with building process chilled water to maintain the desired temperature before entering the module’s distillate channel. The low flow distillate tank was fitted with a pressure transducer (PX309 series, OMEGA Engineering, Stamford, CT) near the bottom to measure the height of the water column. For modules 2 and 3, 757 L feed and distillate conical-bottom tanks were connected to “high flow” (> 4 L/min) positive displacement gear pumps (MAX Series, Liquiflo Chemical Processing Pumps. Garwood, NJ) that circulated each stream according to the same schematic. A radar sensor with a 183cm rod (Model LR3300, LFM electronic, Essen, Germany) measured and recorded the distillate volume for the large reservoirs. For both low flow and high flow experiments, water flux was calculated using the measured change in distillate volume. Resistance thermal detectors (Model EI1034, LabJack Corporation, Lakewood, CO) measured

the temperature at each inlet and outlet of the modules and the three heat exchangers for both the feed and the distillate streams.

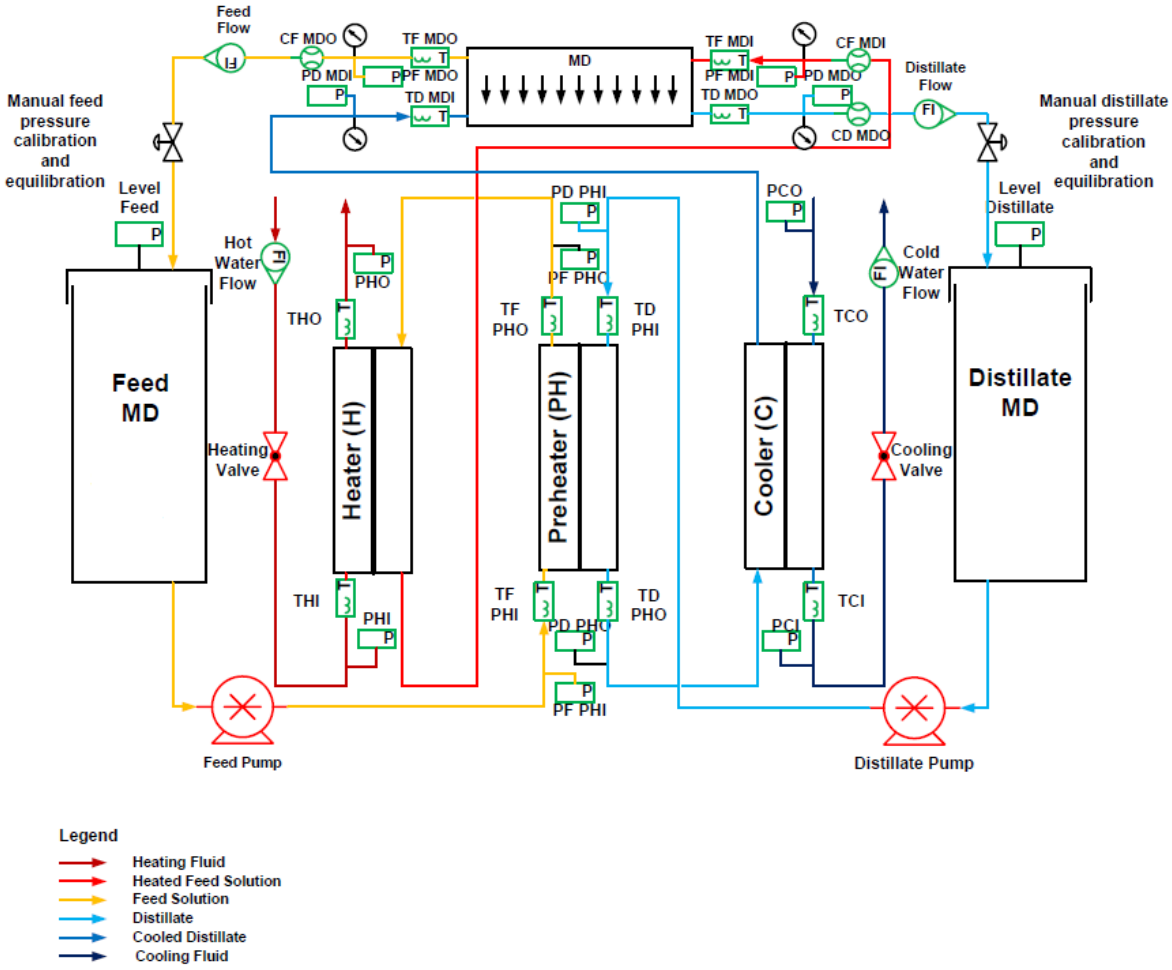

Figure 8. Flow schematic of the pilot scale system for DCMD modules 1 (PFDC) and 2 (SWDC). T = temperature sensor, P=pressure or level sensor, C=conductivity sensor, and F=flow sensor.

Conductivity of the feed and distillate streams were also continuously monitored and recorded, using toroidal sensors (Model TCS3020, TCSTX controlled, Sensorex, Garden Grove, CA) at the feed channel inlet and distillate channel outlet. These values were then used to calculate salt rejection. High conductivity in the distillate stream was also used as an indication of a broken membrane. Pressure transducers (EW- 68075 series, Cole Parmer, Vernon Hills, IL), installed at the inlet and outlet of the module and three heat exchangers, were logged and used to trigger an alarm for a maximum pressure of 69kPa.

For PFAG three channels of 2mm thickness are used. The first channel is a hot stream feed which flows across the membrane. The channel on the other side of the membrane is an air gap separated from the third cold feed stream channel by a 177.8μm thick stainless-steel 304 foil. The distillate produced condenses on the foil in the air gap channel. The distillate runs down the foil normal to the hot and cold feeds. The flow schematic for AGMD is similar to DCMD; however, the preheater was excluded as the module itself functioned as a preheater.

3.5 Model validation experimental design

For each set of experiments, a new dry membrane was cut and installed into Module 1. Modules 2 and 3 were pre-wound and mailed to Golden, Colorado for testing. Feed and distillate solutions were pumped into Module 1 at constant rates of 1L/min or 1.5L/min for each channel while in Modules 2 and 3, nine feed channels and nine distillate channels each received 1.5 L/min. Due to differences in channel dimensions, all three modules were tested at a bulk channel velocity of 0.032m/s. Experiments were performed at two different distillate temperatures of 20 °C or 30 °C, and six different feed temperatures, from 40 to 65°C in increments of 5°C. This results in a total of twelve temperature differences. A summary of the sets of runs is provided in Table 6. V4 has four runs (30-40, 30-45, 30-50, and 30-65) in which the membrane was intentionally wetted. V8 has two repeats of the 20-60 test to assess measurement errors for a total of 14 runs. V10 accomplish PGMD by flooding the air gap chamber. Even though the current model, does not include PGMD, this allows assessment of the sensitivity of PGMD between DCMD and AGMD.

Table 6. Validation case configurations

	Membrane	Flow Rate (L/min)	Flow Config	MD Config	Module	Active Area (m2)	Number of Layers	Number of Tests
V1	CLARCOR QL822	1.5	Counter current	DCMD	1	0.231	1	12
V2	CLARCOR QL822	1.5	Cocurrent	DCMD	1	0.231	1	12
V3*	CLARCOR QL822	1.5	Counter current	AGMD	1	0.231	1	12
V4	Aquastill	13.5	Counter current	DCMD	2	3.6	9	13
V5	Aquastill	2	Counter current	DCMD	1	0.692	2	12
V6	Aquastill	1	Counter current	DCMD	1	0.231	1	12
V7	3M	1	Counter current	DCMD	1	0.231	1	12
V8*	Aquastill	1	Counter current	AGMD	1	0.231	1	14
V9*	Aquastill	13.5	Counter current	AGMD	3	27.4	9	12
V10*	Aquastill	1	Counter current	PGMD	1	0.231	1	12
V11*	3M	1	Counter current	AGMD	1	0.231	1	14

** These cases were not finished or the first run was corrupted by a distillate line leak where humid air entered the line ad brought additional water that was not part of the MD process.*

4 VALIDATION

4.1 Experimental

The comparison between the model and data was made directly with no adjustment to the inputs provided. A significant period of time was invested coming to an understanding of mismatches and many bugs in the model were discovered as a result. Further work might involve optimizing some of the key unknowns in the model to the experimental data.

Numerical testing of the model indicated that five CVPs along the direction of flow was sufficient to meet a convergence criterion of less than 0.03% change in all eleven model outputs analyzed. DCMD therefore only required 5CVPs. For AGMD, three divisions in the gravitational direction produced the same convergence for the distillate film thickness and a total of 15CVPs. The repeated measurements of the V8 20-60 test showed temperature measurement errors less than 1% and mass flow measurement errors less than 2.5% due to process variations.

The gain output ratio (GOR) was calculated as the ratio of the heat of vaporization of all mass transfer to the heat loss from the hot stream.

$$GOR = \frac{\sum_{i=1}^{N_h N_v} \dot{m}_{MD_i} h_v\left(T_{avg_i}\right)}{\sum_{i=1}^{N_v/2} \dot{m}_{h_i} c_P \left(\frac{T_{Ih} + T_{oh_i}}{2}\right)\left(T_{Ih} - T_{oh_i}\right)} \quad (52)$$

With no adjustment to semi-empirical relationships, the comparison of the entire dataset across all configurations is presented in Figure 9. The three outliers for V4 in the GOR plot to the upper left are the three wetted cases (30-40, 30-45, and 30-50). They are also visible in the normalized mass flow plot (middle right) with the greatest downward bias out of the data. On the other hand, the 30-65 wetted case compared with the model almost identically with GOR of 0.659 experimental and 0.698 for MCMD. With only one run, it cannot be determined if this is a change in trend, a measurement error, or a miscommunication of the actual configuration measured. A second GOR anomaly is the V7 case which exhibited much higher normalized mass flow through the membrane than for the experiment than the models prediction. Figure 10 gives the percent error as a function of the input temperature difference across the hot to cold sides and Table 7 gives overall error metrics. Significantly more analysis could be done with the results but these initial comparisons indicate that the model has a 0-7.5% mean bias error and even larger scatter in error.

Table 7. Overall dataset error metrics

	Mean error	Standard deviation of error	Percent mean error	Standard deviation of percent error
GOR	0.002	0.125	4.976	20.352
Hot side temperature out (°C)	2.555	2.954	7.451	8.475
Cold side temperature out (°C)	-0.789	3.016	-1.673	7.215
Normalized mass flow (g/(m^2s))	-0.030	0.292	5.082	26.297
Heat Flow (W/m^2)	-183.541	588.864	-1.720	11.800

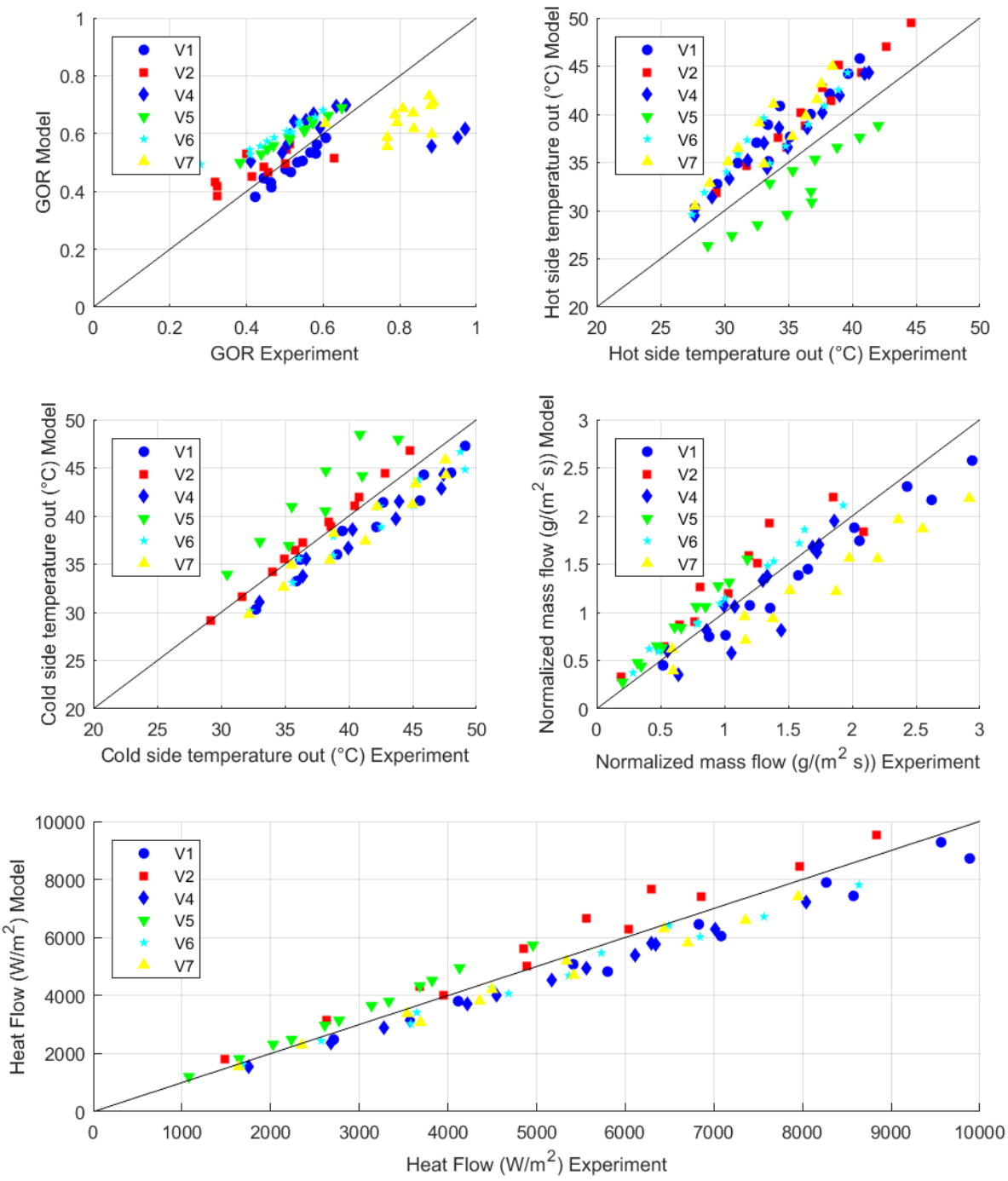

Figure 9. Entire dataset model versus experimental comparison error for GOR, hot side output temperature, cold side output temperature, normalized mass flow, and heat flow.

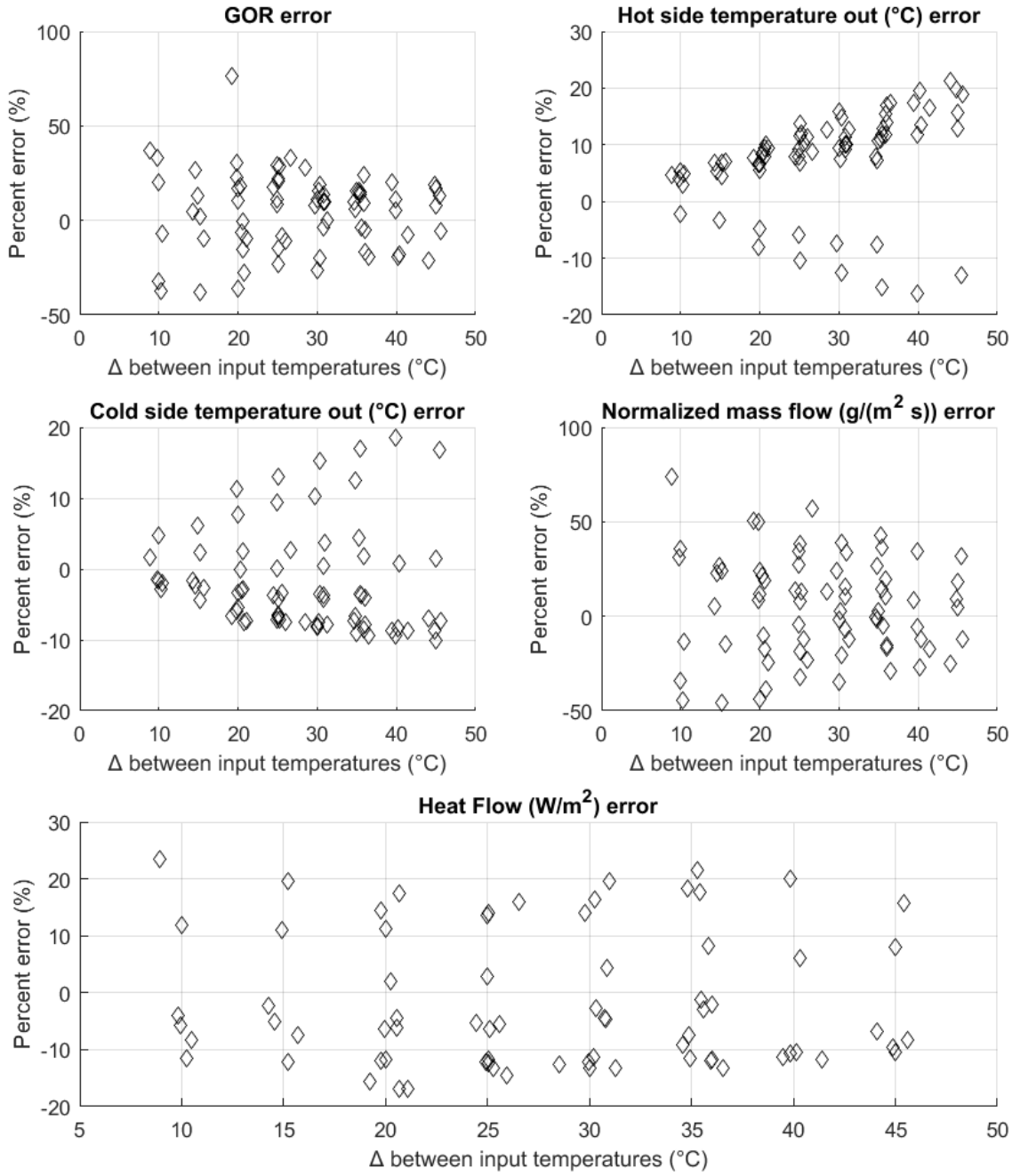

Figure 10. Percent error as a function of the difference between input temperatures.

4.2 Model Based

MCMD was compared to a second single-control volume model developed at NREL in a platform called IPSEpro® to verify whether modeling bugs could be the source of mismatches and to establish the reliability of a lower fidelity DCMD model. A number of bugs in both models were found by this activity until both models fit to each other well as seen for heat transfer in Figure 11. The final differences in models are summarized below in Table 8. Most notable is that the GOR did not match well and could not be reconciled. This is not surprising

given the 5.35% mass flow error and -3.44% heat transfer error. The comparison was made with DCMD using only a single control volume.

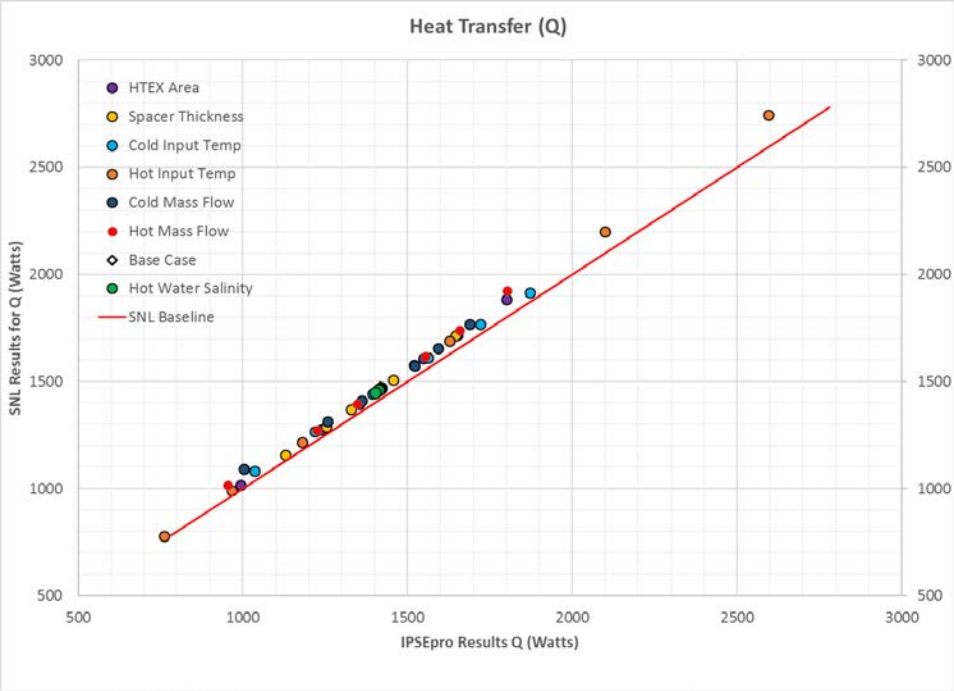

Figure 11. MCMD to IPSEpro model comparison.

Table 8. Difference between IPSEpro and MCMD

Heat Transfer (W)	Distillate mass flow (kg/s)	Membrane Heat Transfer Coefficient (W/m2/K)	HTEX Effectiveness	GOR
-3.44%	+5.35%	-0.15%	+0.20%	+8.50%

5 DISCUSSION

This study was not completed because the AGMD results were found to be corrupted by a hole in the distillate line. Moisture condensed from ambient air and added additional mass flow. As a result, cases V3, V8, and V11 were rejected. Reductions in funding kept cases V9 and V10 from being completed. The dataset presented was not controlled precisely enough to have strong certainty in the model parameters used (Table 5).

We still think that the incorrect datasets are helpful. The wide scatter of data in Figure 9 shows that the stack-up of experimental measurement errors, imprecise synchronization of experiment and model, and modeling limitations create significant uncertainty. Before the experimental error was discovered, the V8 case was one of the best fits as seen below in Figure 12.

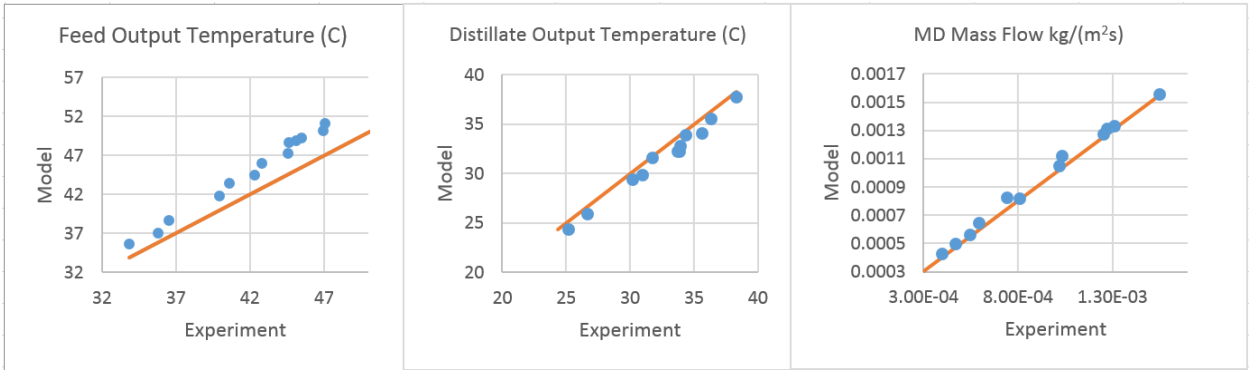

Figure 12 Erroneous V8 results

Many published results in the literature have only as much data as this single case. This brings to remembrance that it is easy to overfit complex models such as MCMD to small amounts of data. The MD modeling community faces the challenge to test their models across many configurations as done in this study so that uncertainty is apparent.

The V11 dataset exhibits the exact behavior expected for a set with additional condensation being added. Figure 13 shows normalized MD mass flow to be linearly biased with experimental data overpredicting with a growing linear trend. This would be expected since the cooling capacity to condense water out of the air will increase in proportion to the AGMD distillates flow rate. From this, we deduce that even though the data has been rejected with an unknown degree of error, that the AGMD portion of MCMD is not that far off. Though errors are greater for other accepted cases, the errors tend to be a near constant bias whereas this case clearly grows linearly.

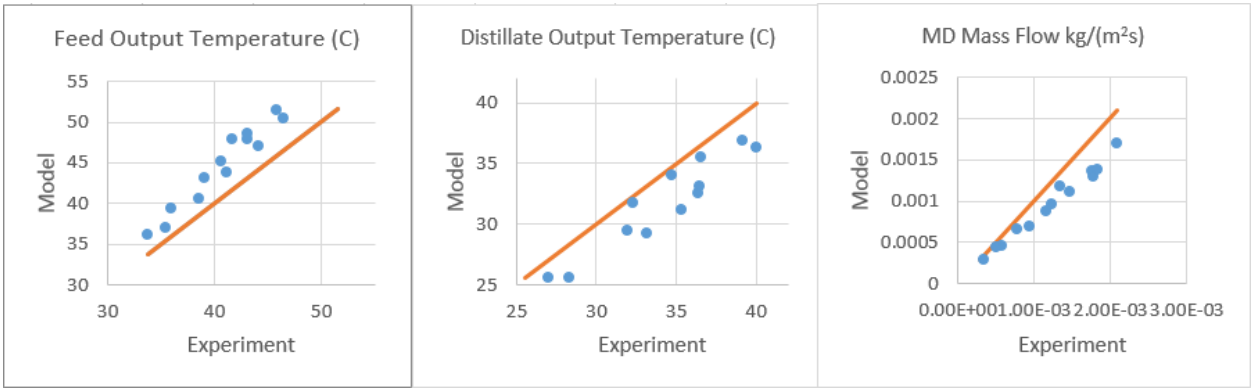

Figure 13. Erroneous V11 data.

The V7 case has the greatest error in mass flow and temperature results among the datasets. This can be explained purely on the basis of inaccurate model inputs—though we do not suspect this is the only cause for the mismatch. As seen in Figure 14, adjustment of physical parameters can make the fit nearly least squares optimal. From this we suspect that the 3M membrane parameters were not well characterized. In general, the mean error in any of these results can be easily reduced to zero through least squares minimization but the scatter in results across all configurations cannot be reconciled completely.

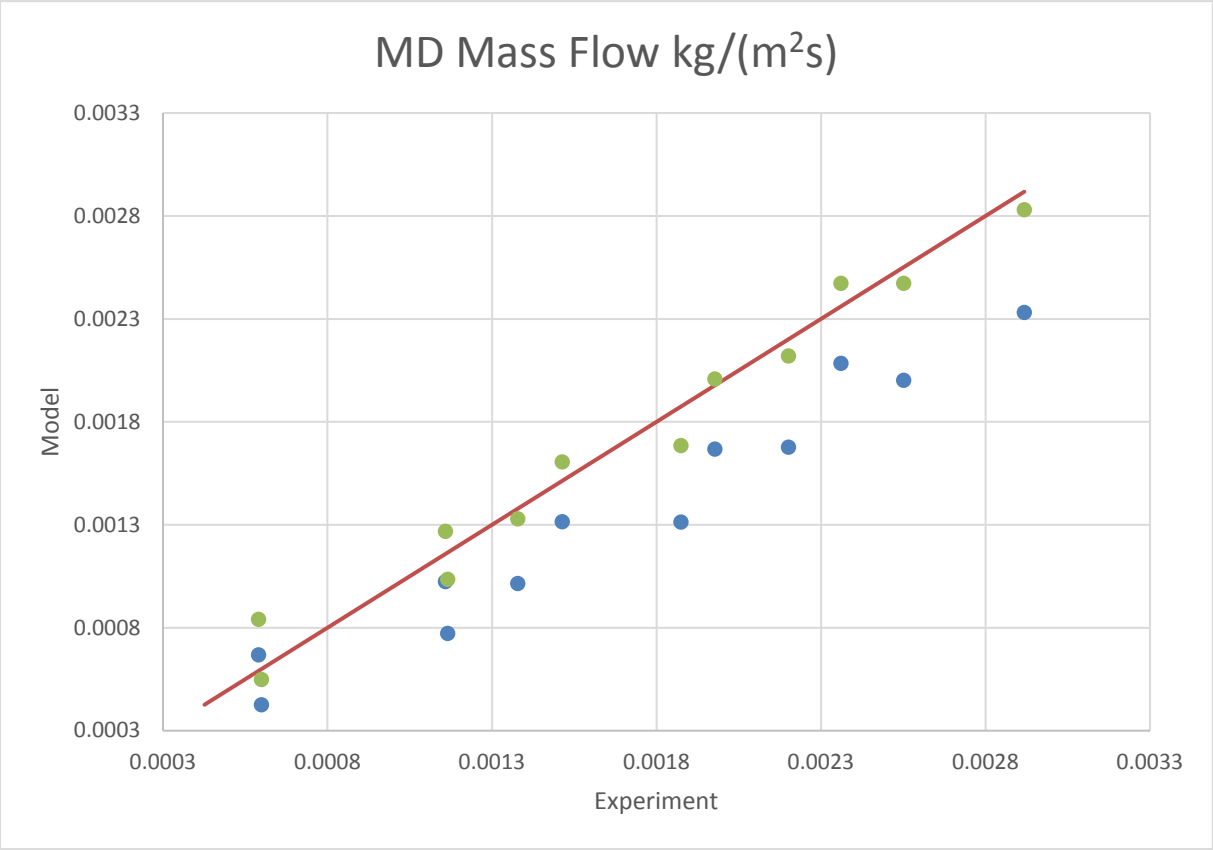

Figure 14. V7 normalized mass flow adjusted to fit data. The porosity was increased to 93%, thickness reduced to 0.05mm, thermal conductivity decreased to 0.1 W/(mK) and mean pore radius increased to 0.0035mm.

The wetted cases also make it clear that many variables exist that can cause the comparison to be unfair. Wetted pores lead to an entirely different set of mass and heat transfer relationships as is clearly seen in three of the wetted cases.

Including the model based IPSIPRO, there is sufficient evidence present to argue that MCMD is well posed for DCMD. This includes the capacity to make predictions for spiral wound and larger flat plate assemblies. Though further verification is needed, a slight correction would infer the same for AGMD.

Even so, we are far from achieving the precision required to verify whether semi-empirical MD models make accurate design comparisons between the MD configurations we have proposed. The high standard deviation error in normalized mass flow of 26.3% in Table 7 is higher than typical design tradeoff decisions where 5-10% resolution is often needed. Figure 10 also shows

that the error grows for output temperatures as the input change in temperature grows. This means the model is less reliable in temperature performance predictions for higher energy systems. This is undesirable for systems process models that may use MCMD. As a result, we think MCMD is best used for estimating MD throughput in low fidelity systems models-where performance is quantified ahead of time and the model is only used to provide reasonable variation. We would advise more caution in using it to choose one MD design over another.

The model based validation was highly useful for finding bugs in MCMD. The low fidelity model's capacity to simulate the MCMD temperature performance makes it evident that MCMD's discretization is hardly necessary for many applications. Even so, MCMD is able to handle much more extreme cases where heat transfer performance becomes nonlinear such as that for an increasingly long heat exchanger as seen in Figure 15. The lower fidelity model cannot reproduce this curve and increased discretization becomes necessary as non-linearity becomes stronger.

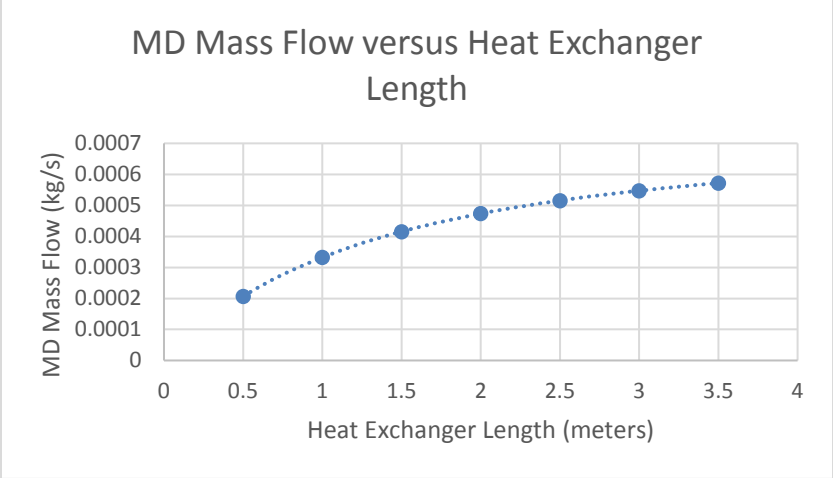

Figure 15. MCMD predicted performance example as a heat exchanger length is increased.

This page intentionally left blank.

6 CONCLUSION

The MCMD model which allows a greater range of configurations to be compared in a common framework has been presented. It has been found that the model reasonably matches experimental data with literature based heat-transfer relationships. It is therefore well suited to single-configuration uses that have been verified to meet the conditions it is simulating. MCMD has been shown to correlate well for lab-scale flat plate assemblies to a full industrial spiral wound module.

Errors across all configurations (~ +/-20%) were considerably higher than typical design comparison performance differences (~5-10%). From this we would suggest that computational fluid dynamics (CFD) is needed to properly compare MD configurations especially when different MD modules are being compared (Shirazi et al., 2016, Hitsov et al., 2015). It is proposed that research toward automating the process of generating Nusselt and Sherwood relationships given changing module configurations using CFD may justify populating MCMD with unique heat and mass transfer relationships for each configuration. MCMD would then provide a low-cost model for design comparisons.

Future work needs to be conducted in order to make this modeling efforts conclusions more quantitative. A multi-variate regression of configuration variables versus change in output variables for the model and for experiments could be used to see if experimentation and modeling come to the same conclusions about design decisions. Accomplishing this will require a more systematic design of experiments with repetition for each run and higher fidelity quantification of model inputs.

This page intentionally left blank.

7 REFERENCES

Alkhudhiri, A., N. Darwish, N. Hilal, 2012. "Membrane distillation: A comprehensive review." *Desalination* 287: 2-18. www.elsevier.com/locate/desal

Alklaibi, A.M. and Noam Lior. 2007. "Comparative Study of Direct Contact and Air-Gap Membrane Distillation Processes." *Industrial and Engineering Chemistry Research*

Alsaadi, A. S., N. Ghaffour, J.-D. Li, S. Gray, L. Francis, H. Maab, G. L. Amy. 2013. "Modeling of air-gap membrane distillation process: A theoretical and experimental study." *Journal of Membrane Science* 445: 53-65.

Ashoor, B. B., S. Mansour, A. Giwa, V. Dufour, S.W. Hasan. 2016. "Principles and applications of direct contact membrane distillation (DCMD): A comprehensive review" *Desalination* 398: 222-246.

Bodel, B.R. 1963. "Distillation of saline water using silicone rubber membrane." United States Patent 3361645 A.

Chafidz, A., S. Al-Zahrani, M.N. Al-Otaibi, C.F. Hoong, T.F. Lai, M. Prabu, 2014. "Portable and integrated solar-driven desalination system using membrane distillation for arid remote areas in Saudi Arabia." *Desalination* 345: 36-49. www.elsevier.com/locate/desal

Chandrasekharam, D., A. Lashin, N. Al Arifi, A. Al Bassam, C. Varun. "Desalination of Seawater using Geothermal Energy to Meet Future Fresh Water Demand of Saudi Arabia." *Water Resources Management* 31 (3): 781-792.

Chiam, Chel-Ken, Rosalam Sarbatly. 2016. "Study of the rectangular cross-flow flat-sheet membrane module for desalination by vacuum membrane distillation." *Chemical Engineering and Processing: Process Intensification* 102:169-185.

Chung, H.W., J. Swaminathan, D.M. Warsinger, J.H. Lienhard V, 2016. "Multistage vacuum membrane distillation (MSVMD) systems for high salinity applications." *Journal of Membrane Science* 497: 128-141. www.elsevier.com/locate/memsci

Deshmukh, Akshay and Menachem Elimelech. 2017. "Understanding the impact of membrane properties and transport phenomena on the energetic performance of membrane distillation desalination." *Journal of Membrane Science* 539:458-474. https://doi.org/10.1016/j.memsci.2017.05.017

Dow, Noel, Stephen Gray, Jun-de Li, Jianhua Zhang, Eddy Ostarcevic, Audra Liubinas, Paul Atherton, Gareth Roeszler, Andrew Gibbs, Mikel Duke. 2016. "Pilot trial of membrane distillation driven by low grade waste heat: Membrane fouling and energy assessment." *Desalination* 391:30-42.

Eykens, L., T. Reyns, K. De Sitter, C. Dotremont, L. Pinoy, B. Van der Bruggen. 2016. "How to select a membrane distillation configuration? Process conditions and membrane influence unraveled." *Desalination* 399:105-115

Goh, P. S., T. Matsuura, A.F. Ismail, N. Hilal, 2016. "Recent trends in membranes and membrane processes for desalination." *Desalination* 391: 43-60. www.elsevier.com/locate/desal

González, Daniel, José Amigo, Francisco Suárez. 2017. "Membrane distillation: Perspectives for sustainable and improved desalination." *Renewable and Sustainable Energy Reviews* 80: 238-259.

Hitsov, I.T., M.K. De Sitter, C. Dotremont, I. Nopens, 2015. "Modelling approaches in membrane distillation: A critical review." *Separation and Purification Technology* 142: 48-64.

Hitsov, I.T., K. De Sitter, C. Dotremont, P. Cauwenberg, I. Nopens. 2017. "Full-scale validated Air Gap Membrane Distillation (AGMD) model without calibration parameters." *Journal of Membrane Science* 533:309-320.

Khayet, M., 2011. "Membranes and theoretical modeling of membrane distillation: A review." *Advances in Colloid and Interface Science* 164: 56-88.

Kraisheh, M., F. Benyahia, and S. Adham. 2012. "Industrial case studies in the petrochemical and gas industry in Qatar for the utilization of industrial waste heat for the production of fresh water by membrane desalination." *Desalination and Water Treatment* 51(7-9): 1769-1775.

Lange, G., G. van Gendt, F. Bollen, W. Heinzl, K. Zhao, T.G. Fane, 2011. "Demonstrating solar driven membrane distillation using Memsys vacuum-multi-effect membrane distillation." *Proceedings of the IDA World Congress on Desalination and Water Reuse* Perth, Australia, September 5-9, 2011. International Desalination Association Topsfield, MA.

Lemmon, E.W., R.T Jacobsen, S.G. Penoncello, and D.G. Friend. 2000. "Thermodynamic Properties of Air and Mixtures of Nitrogen, Argon, and Oxygen from 60 to 2000 K at Pressures to 2000 MPa." *J Phys. Chem. Ref. Data*, 29(3):331-385.

Lemmon, E. W., M. L. Huber, and M.O. McLinden. 2013. "REFPROP Reference Fluid Thermodynamic and Transport Properties." Database 23, Version 9.1 DLL version number 9.1. *National Institute.*

London, T.C., 2000. *Heat Transfer* 2nd ed. Tulsa, OK: Capstone Publishing Corporation.

Martínez-Díez, L. and M. I. Vázquez-González. 1999. "Temperature and concentration polarization in membrane distillation of aqueous salt solutions." *Journal of Membrane Science* 156(2): 265-273. https://doi.org/10.1016/S0376-7388(98)00349-4

Mohamed, Essam Sh., P. Boutikos, E. Mathioulakis, and V. Belessiotis. 2017. "Experimental evaluation of the performance and energy efficiency of a Vacuum Multi-Effect Membrane Distillation system." *Desalination* 408: 70-80. https://doi.org/10.1016/j.desal.2016.12.020

Nayar, Kishor G., Mostafa H. Sharqawy, Leonardo D. Banchik, John H. Lienhard V. 2016. "Thermophysical properties of seawater: A review and new correlations that include pressure dependence." *Desalination* 390:1-24.

Orfi, Jamel, Abdullah Najib, Emad Ali, Abdulhamid Ajbar, Maher AlMatrafi, Mourad Boumaaza, Khalid Alhumaizi. 2017. "Membrane distillation and reverse osmosis based desalination driven by geothermal energy sources." *Desalination and Water Treatment* 76: 40-52.

Ruiz-Aguirre, A. D.-C. Alarcón-Padilla, G. Zaragoza. 2015. "Productivity analysis of two spiral-wound membrane distillation prototypes coupled with solar energy." *Desalination and Water Treatment* 55(10):2777-2785.

Sarbatly, Rosalam and Chel-Ken Chiam. 2013. "Evaluation of geothermal energy in desalination by vacuum membrane distillation." *Applied Energy* 112: 737-746.

Sharqawy, Mostafa H., John H. Lienhard V, Syed M. Zubair. 2010. "Thermophysical properties of seawater: a review of existing correlations and data." *Desalination and Water Treatment* 16 (2010): 354-380. https://doi.org/10.5004/dwt.2010.1079

Shirazi, Mohammad Mahdi A., Ali Kargari, Ahmad Fauzi Ismail, Takeshi Matsuura. 2016. "Computational Fluid Dynamic (CFD) opportunities applied to the membrane distillation process: State-of-the-art and perspectives." *Desalination* 377:73-90.

Swaminathan, Jaichander. Hyung Won Chung, David M. Warsinger, John H. Lienhard V. 2016. "Membrane distillation model based on heat exchanger theory and configuration comparison." *Applied Energy* 184:491-505.

Tsilingiris, P.T. 2008. "Thermophysical and transport properties of humid air at temperature range between 0 and 100°C." *Energy Conversion and Management* 49: 1098-1110

Villa, Daniel L. Charles W. Morrow, Matthew Solom, Brian P. Dwyer. 2017. "Membrane Distillation Modeling Progress Report Fiscal Year 2016." Sandia National Laboratories Report SAND2017-1448. February.

Wang, Peng, Tai-Shung Chung. 2015. "Recent advances in membrane distillation processes: Membrane development, configuration design and application exploring." *Journal of Membrane Science* 474: 39-56.

Zhang, Jianhua, Stephen Gray, Jun-De Li. 2012. “Modeling heat and mass transfers in DCMD using compressible membranes.” *Journal of Membrane Science* 387-388:7-16.

Zhani, K, K. Zarzoum, H. Ben Bacha, J. Koschikowski, and D. Pfeifle. 2015. “Autonomous solar powered membrane distillation systems: state of the art.” *Desalination and Water Treatment* 57 (47-48): 23038-23051.

Zhao, K., W. Heinzl, M. Wenzel, S Büttner, F. Bollen, G. Lange, S. Heinzl, N. Sarda, 2013. “Experimental study of the memsys vacuum multi-effect-membrane-distillation (V-MEMD) module.” *Desalination* 323: 150-160. www.elsevier.com/locate/desal

8 APPENDIX A PHYSICAL PROPERTIES

Table 9. Thermo-physical properties. All relationships throw an error flag in the model if used outside of its valid range

Property	Equation	Reference/Bounds
Specific heat of liquid water (J/(kg·K))	$c_P(T,S) = 1000(A + BT + CT^2 + DT^3)$ $A = 5.328 - 0.0976S + 0.000404S^2$ $B = -0.006913 + 0.0007351S - 3.15e\text{-}6S^2$ $C = 9.6e\text{-}6 - 1.927e\text{-}6S + 8.23e\text{-}9S^2$ $D = 2.5e\text{-}9 + 1.666e\text{-}9S - 7.125e\text{-}12S^2$	Sharqwy et al. (2010) $273 < T < 453K$ $0 < S < 180g/kg$
Saline Water Saturated Vapor Pressure (Pa)	$P_{sat}(T,S) = P_{Tv}(T)e^{[-4.5818e-4S-2.0443e-6S^2]}$ $P_{Tv}(T) = e^{\left[\frac{-5800}{T}+1.3915-0.04864T+4.1765e-5T^2-1.4452e-8T^3+6.546\log(T)\right]}$	Nayar et al. (2016) $273 < T < 453K^*$ $0 < S < 0.16$
Thermal conductivity of liquid saline water (W/(m·K))	$k(T,S) = \frac{10^{\frac{\ln(240+.0002S)}{\ln(10)}+0.434\left(2.3-\left(\frac{343.5+0.037S}{T+273.15}\right)\right)\left(1-\left(\frac{T+273.15}{647+0.03S}\right)\right)^{0.333}}}{1000}$	Sharqwy et al. (2010) $0 < T < 180°C$ $0 < S < 160g/kg$
Density of liquid saline water (kg/m³)	$\rho(T,S) = 999.9 + 0.02034T - 6.162e\text{-}3T^2 + 2.261e\text{-}5T^3 - 4.657e\text{-}8T^4 + 802S - 2.001ST + 0.01677ST^2 - 3.06e\text{-}05ST^3 - 1.613e\text{-}5S^2T^2$	Sharqwy et al. (2010) $0 < T < 180°C$ $0 < S < .160$
Dynamic Viscosity of liquid, saline water (Pa·s)	$A = 0.001474 + 1.5e\text{-}5T - 3.927e\text{-}8T^2$ $B = 1.073e\text{-}5 - 8.5e\text{-}8T + 2.23e\text{-}10T^2$ $\mu_w(T) = e^{-10.7019+\frac{604.129}{139.18+T}}$ $\mu(T,S) = \mu_w(T)(1 + AS + BS^2)$	Sharqwy et al. (2010) $0 < T < 180°C$ $0 < S < 150g/kg$
Prandtl number of dry air at 1atm	$Pr_a(T) = 0.8927 - 2.118e\text{-}3T + 1.211e\text{-}5T^2 - 4.26e\text{-}8T^3 + 8.822e\text{-}11T^4 - 9.756e\text{-}14T^5 + 4.464e\text{-}17T^6$	Fit created in this work data from Lemmon et al. (2013) $200 < T < 450K$

* Even though the original publication indicates °C, Kelvin works after validation.

Thermal diffusivity of dry air at 1atm (m^2/s)	$\alpha_a(T) = -1.325e\text{-}9T^3 + 2.805e\text{-}6T^2 + 3.812e\text{-}5T - 5.343e\text{-}3$	Fit created in this work data from Lemmon et al. (2000) $200 < T < 450K$
Kinematic viscosity of dry air at 1 atm (m^2/s)	$\nu_a(T) = (-5.447e\text{-}10T^3 + 1.574e\text{-}6T^2 + 1.381e\text{-}4T - 0.0109)/1e4$	Fit created in this work data from Lemmon et al. (2000) $200 < T < 450K$
Thermal conductivity of dry air (W/(m·K))	$k_a(T) = 4.349e\text{-}11T^3 - 7.976e\text{-}8T^2 + 1.104e\text{-}4T - 7.323e\text{-}4$	Fit created in this work data from Lemmon et al. (2000) $200 < T < 450K$
Heat of vaporization of water (J/kg)	$h_v(T) = 4.244030e\text{-}6 - 19679.4T + 114.29T^2 - 0.406878T^3 + 8.26231e\text{-}4T^4 - 8.97818e\text{-}7T^5 + 3.92177e\text{-}10T^6$	Fit created in this work data from Lemmon et al. (2013) $275 < T < 475K$
Thermal conductivity of a saturated air water mixture (W/(m·K))	$k_{av}(T,P) = \frac{k_a(T)x_a}{x_a + x_v(T,P)\Psi_{av}(T,P)} + \frac{k_v(T)x_v(T,P)}{x_v(T,P) + x_a\Psi_{va}(T,P)}$ $\Psi_{av}(T,P) = 2^{-1.5}\left(1 + \frac{1}{M_{ratio}}\right)^{-0.5}\left(1 + \mu_{ratio}(T,P)^{0.5}M_{ratio}^{0.25}\right)^2$ $\Psi_{va}(T,P) = 2^{-1.5}(1 + M_{ratio})^{-0.5}\left(1 + \mu_{ratio}(T,P)^{-0.5}M_{ratio}^{-0.25}\right)^2$ $M_{ratio} = 0.622$ $\mu_{ratio}(T,P) = \frac{\mu_a(T,P)}{\mu_v(T)}$ $x_a = 1 - x_v(T,P)$	Tsilingiris (2008) $0 < T < 100°C$

Water vapor thermal conductivity (W/(m·K))	$k_v(T) = 17.61758242 + 0.05558941059T + 1.663336663e\text{-}4T^2$	Tsilingiris (2008) $0 < T < 120°C$
Water Vapor Mole fraction for saturated air	$x_v(T,P) = f\left(T,P,P_{sat}(T)\right)\frac{P_{sat}(T)}{P}$ $f\left(T,P,P_{sat}(T)\right) = e^{\left(x_{i1}(T)\left(1-\frac{P_{sat}(T)}{P}\right)+x_{i2}(T)\left(\frac{P_{sat}(T)}{P}-1\right)\right)}$ $x_{i1}(T) = 3.53624e\text{-}4 + 2.93228e\text{-}5T + 2.61474e\text{-}7T^2 + 8.57538e\text{-}9T^3$ $x_{i2}(T) = e^{-10.7588+0.0632529T-2.53591e\text{-}4T^2+6.33784e\text{-}7T^3}$	Tsilingiris (2008) $0 < T < 100°C$ Pressure range not known. Must be near 1atm
Dry air dynamic viscosity (Pa·s)	$\mu_a(T,P) = 4.812152422e\text{-}6 + 4.5733595e\text{-}8T + 1.354851553e\text{-}13P$	Fit created in this work data from Lemmon et al. (2000) $280 < T < 400K$ $0.1 < P < 1e6Pa$
Water vapor dynamic viscosity (Pa·s)	$\mu_v(T) = 1e\text{-}6(8.058131868 + 0.04000549451T)$	Tsilingiris (2008) $0 < T < 120°C$ Original equation was off by a factor of 10.
Saturated water vapor enthalpy (J/kg)	$h_{wv}(T) = 691373990 - 15143123.2T + 146423.801T^2 - 817.719281T^3 + 2.90724215T^4 - 6.82487784e\text{-}3T^5 + 1.05809713e\text{-}5T^6 - 1.04491551e\text{-}8T^7 + 5.96598746e\text{-}12T^8 - 1.50094973e\text{-}15T^9$	Fit created in this work data from Lemmon et al. (2013) $275 < T < 600K$
Saturated liquid water enthalpy (J/kg)	$h_{wl}(T) = -464010550 + 10159037.8T - 98057.4908T^2 + 547.007459T^3 - 1.94286618T^4 + 4.55698146e\text{-}3T^5 - 7.05941371e\text{-}6T^6 + 6.96646051e\text{-}9T^7 - 3.97478846e\text{-}12T^8 + 9.99299563e\text{-}16T^9$	Fit created in this work data from Lemmon et al. (2013) $275 < T < 600K$

Solute diffusivity of saline water (m^2/s)	$$D_{sw}(T,S) = 8.928 \times 10^{-10} T^o \left(\frac{\frac{1}{n_-}+\frac{1}{n_+}}{\frac{1}{\lambda_-}+\frac{1}{\lambda_+}}\right)\left(\frac{T}{334,000 \cdot \mu(T,S)}\right)$$ $$T^o = 298.15K, \lambda_- = 0.007634 \frac{Siemen \cdot m^2}{mol}, \lambda_+ = 0.005011 \frac{Siemen \cdot m^2}{mol}$$ $$n_- = n_+ = 1$$ λ is the limiting molar ionic conductances for the anion (-) and cation (+). n is the valence of Cl and Na.	Chiam and Sarbatly (2016) Range of validity not known. Assume range of validity of the viscosity.

9 APPENDIX B - USING MCMD

MCMD is open-source software that runs in Excel®. It has been posted to GitHUB at the following site: https://github.com/dlvilla/MCMD1. Anyone is welcome to use any part of the code as long as they read and comply with the BSD-3 clause copyright statement. The visual basic for applications (VBA) code within the spreadsheet is best used programmatically but a basic interface has been added to allow single runs to be made and results viewed as seen in Figure 16 and Figure 17. The drop down menus are populated with entries in the "Water Streams," "Spacers," and "Membrane and Foils" sheets. It is advisable to use the model through VBA as instructed on the "Help" sheet.

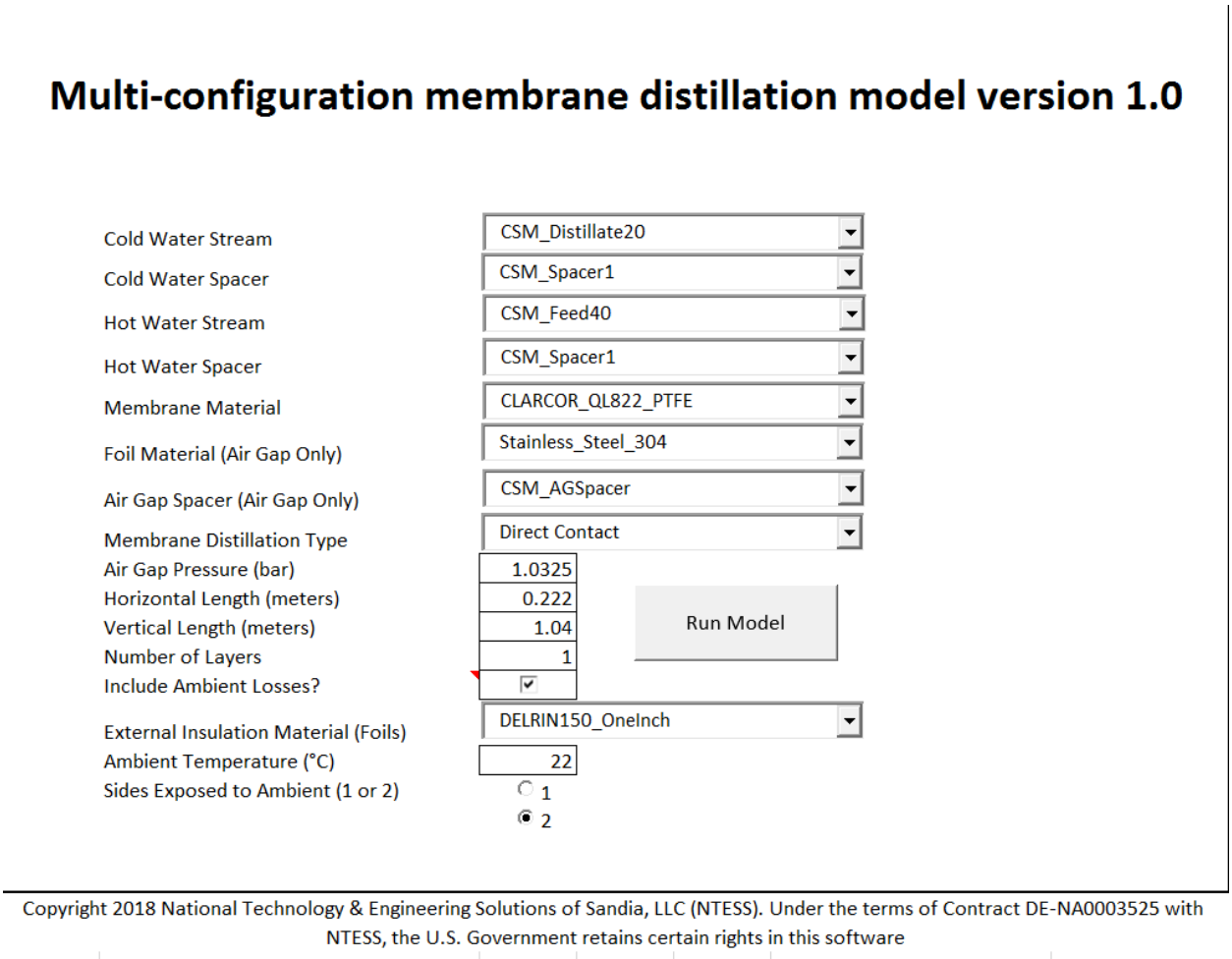

Figure 16. MCMD single run interface input sheet.

Multi-configuration membrane distillation (MCMD) model version 1.0

Output	Value	Units	Value	Notes
Total MD mass flow rate:	0.00053	kg/s	1.93991	liter/hour
Gain Output Ratio (GOR)	0.5854			
Cold Input Temperature	30.3288	°C		
Average Cold Output Temperature	49.765	°C		
Hot Input Temperature	65.9239	°C		
Average Hot Output Temperature	45.7837	°C		
Total Heat Flow Through Membrane	2143.08	Watts		
Total Heat Losses to Ambient	38.5624	Watts		
Heat Transfer Due to Mass Transfer	1269.88	Watts		
Conduction Heat Transfer Through Membrane	873.205	Watts		
Percent Heat Losses	1.80%			
Hot Mass Flow Out	0.02404	kg/s		
Hot Salinity Out	0.00409	kg/kg		
Cold Mass Flow Out	0.02542	kg/s		
Cold Salinity Out	0	kg/kg		

Flow Path Relative Length	Average Cold Stream Temperature	Flow Path Relative Length	Average Hot Stream Temperature
0	303.4788186	0	339.0739384
0.2	306.9564563	0.2	334.5947916
0.4	310.6227879	0.4	330.3563266
0.6	314.4938134	0.6	326.3436437
0.8	318.5858581	0.8	322.5412616
1	322.9149751	1	318.933741

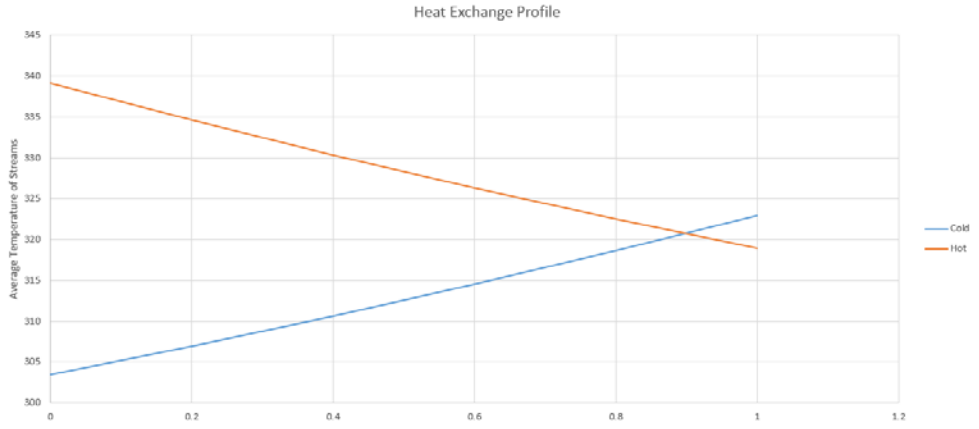

Figure 17. MCMD single run interface output sheet.

DISTRIBUTION

2 National Renewable Energy Laboratory
Attn: Craig Turchi craig.turchi@nrel.gov (electronic copy)
15013 Denver West Parkway
Golden, CO 80401

1 Colorado School of Mines
Department of Civil and Environmental Engineering
Attn: Tzahi Y. Cath tcath@mines.edu (electronic copy)
Coolbaugh Hall
1012 14th St.,
Golden, CO 80401

1	Johan Vanneste	Colorado School of Mines	vanneste@mines.edu (electronic copy)
1	Sara Emmons	Department of Energy Geothermal Technologies Office	Sara.emmons@ee.doe.gov (electronic copy)
1	David Jassby	University of CA Riverside	djassby@engr.ucr.edu (electronic copy)
1	Sertac Akar	NREL	Sertac.Akar@nrel.gov (electronic copy)

1	MS0747	Leigh Cunningham	08843 (electronic copy)
1	MS0747	Charles Morrow	08843 (electronic copy)
1	MS0747	Geoffrey A. Freeze	08843 (electronic copy)
1	MS0754	Brian Dwyer	08862 (electronic copy)
1	MS1138	Daniel Villa	06926 (electronic copy)
1	MS1138	Stephanie Kuzio	06926 (electronic copy)
1	MS0899	Technical Library	09536 (electronic copy)

This page intentionally left blank.

Sandia National Laboratories